



UNIVERSITÀ POLITECNICA DELLE MARCHE
Repository ISTITUZIONALE

Risk Assessment of Reinforced Concrete Buildings with Rubber Isolation Systems Designed by the Italian Seismic Code

This is the peer reviewed version of the following article:

Original

Risk Assessment of Reinforced Concrete Buildings with Rubber Isolation Systems Designed by the Italian Seismic Code / Micozzi, F.; Flora, A.; Viggiani, L. R. S.; Cardone, D.; Ragni, L.; Dall'Asta, A. - In: JOURNAL OF EARTHQUAKE ENGINEERING. - ISSN 1363-2469. - ELETTRONICO. - 26:14(2022), pp. 7245-7275. [10.1080/13632469.2021.1961937]

Availability:

This version is available at: 11566/299442 since: 2024-04-27T16:34:45Z

Publisher:

Published

DOI:10.1080/13632469.2021.1961937

Terms of use:

The terms and conditions for the reuse of this version of the manuscript are specified in the publishing policy. The use of copyrighted works requires the consent of the rights' holder (author or publisher). Works made available under a Creative Commons license or a Publisher's custom-made license can be used according to the terms and conditions contained therein. See editor's website for further information and terms and conditions.

This item was downloaded from IRIS Università Politecnica delle Marche (<https://iris.univpm.it>). When citing, please refer to the published version.

(Article begins on next page)

**Risk assessment of Reinforced Concrete buildings with Rubber
Isolation Systems designed by the Italian Seismic Code**

F. Micozzi¹, A. Flora², L.R.S. Viggiani², D. Cardone², L. Ragni³, A.
Dall'Asta¹

¹School of Architecture and Design, University of Camerino, Camerino, Italy

e-mail: fabio.micozzi@unicam.it, andrea.dallasta@unicam.it,

²School of Engineering, University of Basilicata, Potenza, Italy

e-mail: amedeo.flora@unibas.it, donatello.cardone@unibas.it, luciano.viggiani@unibas.it

*³Department of Civil and Building Engineering and Architecture, Università Politecnica delle
Marche, Ancona, Italy*

e-mail: laura.ragni@univpm.it

Risk assessment of Reinforced Concrete buildings with rubber isolation systems designed by the Italian Seismic Code

ABSTRACT

This paper presents an insight on the seismic response and seismic risk of base-isolated structures performed within the RINTC project, considering different configurations of rubber-based isolation systems. This represents an in-depth revision of past works [*Ragni et al. 2018a*, *Cardone et al. 2019b*] due to the adoption of more robust and accurate isolator model. Four archetype 6-storeys RC frame buildings are examined, representing both new designed isolated buildings and existing buildings retrofitted with seismic isolation, differing in age of construction and location (the cities of L'Aquila (central Italy) and Naples (southern Italy)). All the isolation systems are designed in accordance with the current Italian Seismic Code. Seismic performance assessment is performed by multi-stripe nonlinear time history analysis. The annual failure rates for two different performance levels, namely Global Collapse and Usability Preventing Damage, are computed. The results point out that all isolation systems work effectively in limiting damage while they show a quite low margin with respect to collapse, regardless of the dominant failure mode, which is governed by the more fragile component among isolation system and superstructure. The annual failure rates derived for base-isolated buildings are critically reviewed and then compared with those obtained for similar new designed fixed-base RC buildings.

KEYWORDS

Base isolation, high damping rubber bearings, seismic performance, multi-stripe analyses, risk assessment, annual failure rate

2 **Introduction**

3 In the last decades, the base isolation technique [*Naeim and Kelly, 1999*] has emerged
4 as an attractive strategy for both the seismic design of new buildings and the seismic retrofit of
5 existing buildings. Several numerical studies and the experience derived from recent seismic
6 events have definitely demonstrated the applicability of base isolation for the seismic protection
7 of buildings.

8 So far, only a few studies have focused on the collapse performance of seismically iso-
9 lated structures and, as a consequence, on the assessment of the safety margins against collapse
10 [*Cardone et al. 2019a, Kitayama and Constantinou 2018, Kitayama and Constantinou 2019,*
11 *Shao et al. 2019*]. Among those, the authors of this paper already investigated the seismic per-
12 formances of RC frame buildings equipped with rubber-based isolation systems [*Ragni et al.,*
13 *2018a, Cardone et al., 2019b*], towards two different performance levels (i.e. Global Collapse
14 (GC) and Usability-Preventing Damage (UPD) performance levels), via Multi-Stripe nonlinear
15 dynamic Analyses (MSAs) [*Jalayer, 2003, Scozzese et al., 2020*]. In the mentioned studies, car-
16 ried out within the *RINTC* (Implicit Risk of code-conforming Italian buildings) research project
17 [*ReLUIIS-RINTC, 2018, Iervolino and Dolce, 2018*], reference to two sites, characterized by dif-
18 ferent seismic hazard (i.e. L'Aquila and Naples), both on soil type C (medium soft soil), has
19 been made. The outcomes have been then used as input for the subsequent evaluation of the rel-
20 evant implicit risk of failure within a probabilistic framework [*Iervolino et al., 2018*].

21 The results presented in [*Ragni et al., 2018a, Cardone et al., 2019b*] outlined that, re-
22 gardless of the characteristics of the superstructure (new or existing, namely retrofitted), the
23 rubber-based isolation systems work effectively in limiting damage in non-structural compo-
24 nents up to seismic intensities much higher than the relevant design earthquake intensity level.
25 As a consequence, the annual failure rates associated with the *UPD* performance level, observed
26 for base-isolated buildings, are lower than those obtained for fixed-base structures [*Iervolino et*
27 *al., 2018*]. On the other hand, a little margin to collapse (beyond the design earthquake intensity

level) has been observed for base-isolated buildings, thus leading to collapse failure rates very similar to (or even greater than) those for fixed-base structures.

In the mentioned past studies, the nonlinear 3D models of base-isolated buildings have been implemented in the OpenSees framework [McKenna, 2011] using the *HDR Bearing Element* [Kumar et al., 2014] to describe the cyclic behaviour of rubber isolators. The *HDR Bearing Element* is characterized by a very advanced horizontal behaviour (in shear) able to capture the first cycle stiffness and the softening behaviour due to repeated cycles; however, it does not account for the post-buckling response characterized by the reduction of the horizontal stiffness due to vertical loads. On the other hand, the *ElastomericX* element (already implemented in OpenSees by the same Authors of *HDR Bearing Element*) is based on a simpler shear behaviour and on a simplified method to predict the reduction of the horizontal stiffness due to vertical loads. However, the *ElastomericX* element is specific for low damping rubber bearings and is not able to properly describe the cyclic behaviour of high damping rubber bearings.

Recently, a new model for *HDRB* isolators, referred to as *Kikuchi Bearing Element* [Ishii and Kikuchi, 2019], has been proposed and implemented in OpenSees. It represents an upgrade of the very preliminary version proposed in [Yamamoto et al., 2009]. The *Kikuchi Bearing Element* is a two-nodes link element with multi-spring mechanical model which includes two sets of multiple axial springs and a set of mid-height multiple (radial) shear springs. Each radial spring is characterized by the *KikuchiAikenHDR* uniaxial material [Kikuchi and Aiken, 1997]. The springs are bound together by rigid links, according to the older *two spring model* formulation [Koh and Kelly, 1988, Koh and Kelly 1986]. The main advantage of the *Kikuchi Bearing Element* is represented by the possibility of capturing the axial-shear load interaction for small and large displacements and, as a consequence, the associated pre- and post-buckling behaviour. As a result, the *Kikuchi Bearing Element* model is able to capture the effective horizontal stiffness of the isolators as well as its variability due to rocking effects of the superstructure during an earthquake. A synthetic comparison of the two bearing elements is reported in Table 1.

Table 1. Features comparison of the *HDR Bearing Element* and the *Kikuchi Bearing Element*

<i>Features</i>	<i>HDR Bearing Element</i> [Kumar et al. 2014]	<i>Kikuchi Bearing Element</i> [Ishii and Kikuchi, 2019]
Coupled bidirectional horizontal model	✓	✓* (multi-shear spring)
Shear degradation due to Mullins effect	✓	✗
Coupled horizontal-vertical behaviour: Vertical stiffness reduction due to horizontal displacement	✓	✓
Coupled horizontal-vertical motion: horizontal stiffness reduction due to vertical load and horizontal displacement	✗	✓
Cavitation and post-cavitation effects	✓	✓
Cyclic and degrading hysteresis behaviour in cavitation and post-cavitation	✓	✗
Post-buckling behaviour	✗	✓

A further difference that should be remarked is that the *Kikuchi Bearing Element* has a reduced number of calibration parameters for the horizontal behaviour with respect to *HDR Bearing Element*, thus simplifying the calibration procedure (even if there are some limitation for hardening behaviour calibration).

The main novelties of the present study are: (i) the calibration of the *Kikuchi Bearing Element*, based on fitting of experimental data, specifically relevant to commercial devices currently used in Italy; (ii) the performance assessment, via *MSAs* (for both *UPD* and *GC* performance levels), of several case studies of new and existing buildings retrofitted with rubber-based isolation systems, using the *Kikuchi Bearing Element*; (iii) the calculation and critical examination of the corresponding annual failure rates (for both *UPD* and *GC*), (iv) the comparison between new and retrofitted buildings with base isolation, in terms of structural performances and failure rates and (v) the comparison between base-isolated and similar new designed fixed-base RC buildings.

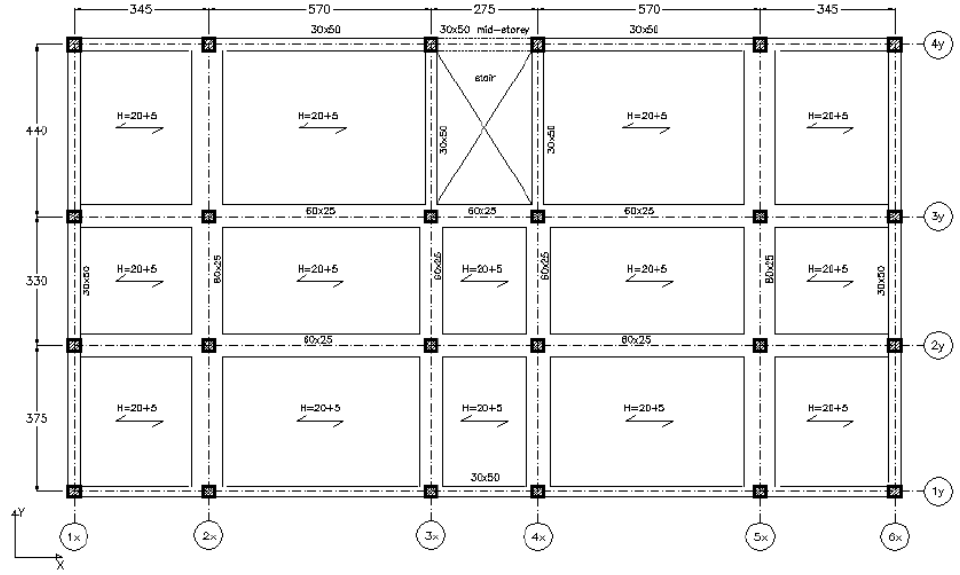
Case studies

Archetype Buildings

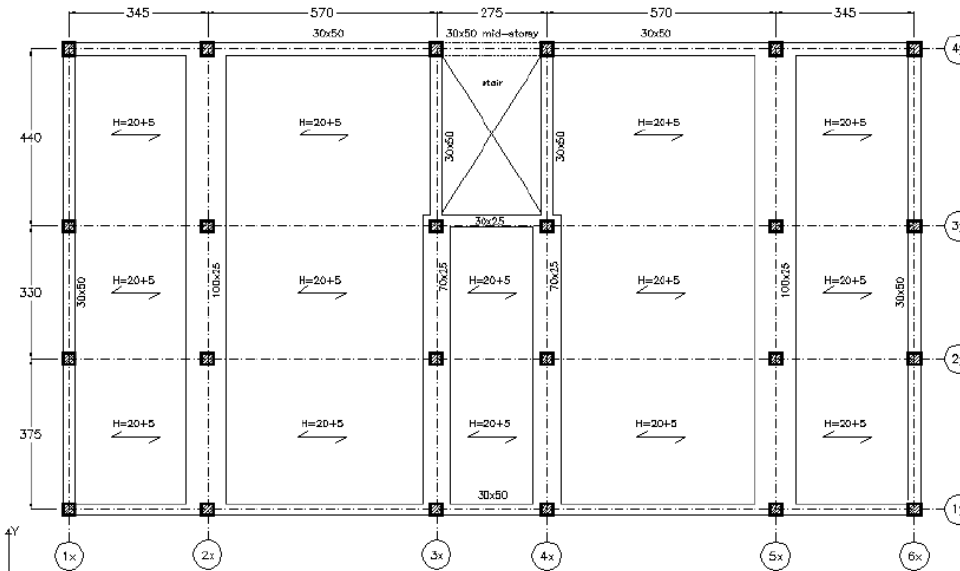
The examined (new and existing) buildings are located in two different sites (namely, the city of Naples, southern Italy, and the city of L'Aquila, central Italy), characterized by medium and

high seismicity for Italy, respectively. All buildings are intended for residential use, featuring a regular plan of approximately 240 square meters and 6 stories above ground. The ground level height is equal to 3.4 m while that of all the other stories is equal to 3.05 m. The building structure includes knee beams staircase. All floor plans are identical except for columns and beams dimensions and reinforcements.

The existing buildings have been defined in a previous study [Ricci et al., 2019] by means of simulated design, in accordance with outdated Italian Seismic Codes. In particular, the building located in Naples (labelled as NA_{EX} in what follows) has been designed for gravity loads only (Gravity Loads Design, GLD) according to [D.M. 30/5/1974]; The building located in L'Aquila (labelled as AQ_{EX} in the following), has been defined based on a simulated seismic load design (Seismic Load Designed, SLD), considering low seismic forces, according to past seismic classifications [D.M. 14/2/1992], and outdated technical regulations [D.M. 24/1/1986]. Figure 1 shows the typical floor plan of the (a) AQ_{EX} building and (b) NA_{EX} building. In both cases the outer beams are all deeper than the slab, while all internal beams are flat. In the NA_{EX} building, the internal beams are positioned only in the y-direction. All the stories feature the same slab, whose total thickness is equal to 250mm (including hollow bricks). It is worth noting that in the base-isolated configuration, a supplementary floor has been added at the bottom of the first storey columns and a grid of RC beams has been implemented at the same level. According to the technical practice of the period, masonry infills featuring a double layer (120+80 mm thickness) of hollow clay bricks, with 100 mm inner cavity, have been considered. More details about the existing buildings (i.e. cross-section dimensions, reinforcement ratios, material properties etc.) can be found in [Ricci et al., 2019].



(a)



(b)

Figure 1. Floor plan for (a) AQ_{EX} and (b) NA_{EX} existing archetype buildings.

The seismic design of the new base-isolated buildings has been performed based on linear dynamic analyses according to the current Italian Seismic Code called *NTC2018* [CS.LL.PP., 2018] and its explicatory notes [CS.LL.PP., 2019]. The superstructure of the new base-isolated buildings (AQ_{NEW} and NA_{NEW}) features four frames in the long (X-) direction and six external frames in the short (Y-) direction (see Figure 2). The masonry walls, realized with a single layer

(300 mm thickness) of hollow clay bricks, are regularly distributed in plan and elevation, featuring different percentages of openings. A good connection of the infill panels with the RC frame has been assumed in the numerical model for the performance assessment. Structural elements' dimensions and reinforcements have been defined and verified according to the prescriptions provided by the current version of the Italian Seismic Code [CS.LL.PP., 2018, Chpt. 7.10.4.2]. More details about the structural details and masonry infill characteristics of the new base-isolated buildings can be found in [Ragni et al., 2018a].

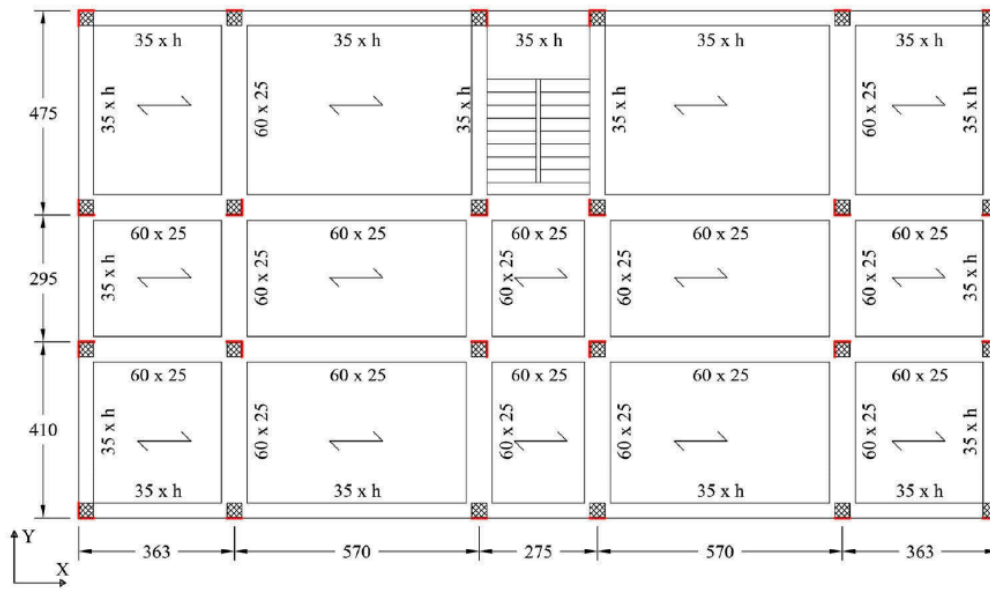


Figure 2. Floor plan for new isolated buildings.

Seismic Hazard

The hazard model adopted in the present study has been defined based on a preliminary Probabilistic Seismic Hazard Analysis (PSHA) performed using OPENQUAKE [Monelli et al., 2012]. The spectral acceleration, $S_a(T^*)$, associated with a suitable conditioning period, T^* , has been assumed as Intensity Measure (IM) to derive the hazard curves for the building sites. For the sake of clarity and accuracy, the conditioning period used to define the IM has been chosen as close as possible to the design value of the effective fundamental period of each base-isolated building. Hazard curves have been discretized in ten Intensity Measure (IM) levels, corresponding to the following Return Periods (RPs): 10, 50, 100, 250, 500, 1000, 2500, 5000, 10000 and 100000 years. The first 7 levels (from 1 to 7) correspond to Return Periods values typically adopted by

the current Italian Seismic Code for site hazard curves. In order to properly assess the safety margins against collapse and estimate an annual exceedance rate down to 10^{-5} , three additional larger hazard levels have been included (corresponding to Return Periods equal to 5000, 10000 and 100000 years, respectively) [Iervolino *et al.*, 2018]. Subsequently, the Conditional Spectrum (CS) method [Lin *et al.* 2013, NIST 2011], combined with a post processing procedure ensuring consistency of selected records with magnitude-distance disaggregation [Spillatura, 2018], has been used to select 20 seismic records pairs for each *IM*. All the information about seismic hazard assessment and record selection can be found in [Iervolino *et al.*, 2018] and have been carried out within the *RINTC* project for different building typologies, including the base-isolated buildings under consideration. It is worth noting that, while the Ground-Motion Prediction Equation (*GMPE*) selected for computing the seismic hazard for fixed-base RC buildings (featuring fundamental periods lower than 2.0 s) is that proposed by [Ambraseys *et al.*, 1996], the *GMPE* by [Akkar and Bommer, 2010] has been employed for predicting the response of base-isolated structures, characterized by longer fundamental periods (of the order of 3.0 s). As a matter of fact, indeed, the *GMPE* by [Ambraseys *et al.*, 1996] is not suitable for base-isolated buildings being limited to a maximum period equal to 2.0 s. Specific considerations about the effects (on the failure rate for the *GC* performance level) of changing the *GMPE* for base-isolated structure are provided in the last section (Risk Assessment) of the paper.

Isolation System

Two different typologies of rubber-based isolation systems have been considered herein for both new and existing buildings. In particular, the first typology (labelled as *HDRB*) is composed by High Damping Rubber Bearings only (*HDRBs*) while, the second typology (labelled as *HDRB+FSB*) is based on a proper combination of *HDRBs* (placed below the columns along the perimeter of the building) and Flat Sliding Bearings (*FSBs*) (placed below the inner columns of the building). The catalogues of the main Italian manufacturers have been used to select commercial devices, featuring suitable values of effective stiffness and vertical capacity. The seismic design of the mentioned isolation systems has been performed through modal response

spectrum analysis, in accordance with the latest release of the Italian Seismic Code [CS.LL.PP., 2018, 2019].

Two different approaches have been followed for the design of the rubber-based isolation systems for new and existing buildings, respectively, according the current technical practice in Italy [Dolce et al. 2010]. For the latter, the design approach consists in limiting the seismic force transmitted to the superstructure under the “elastic” limit of the superstructure, defined by means of Push Over Analysis (POA), thus avoiding the structural damage up to the design earthquake intensity level associated with the Life-safety Limit State (LLS). The elastic limit, in terms of base shear (V_y), of the superstructure (in the fixed-base configuration) has been identified in the PO curves as the force level corresponding to the occurrence of the first plastic hinge in the weaker direction of the building (i.e. the minimum base shear at the first yielding), as shown in Figure 3 (a) and (b). Once the elastic limit has been identified, the target fundamental period of the base-isolated building has been derived (Figure 3 (c)) and the corresponding value of the maximum displacement (S_{dmax}) has been evaluated using the displacement spectrum associated with the Collapse Limit State (CLS) (Figure 3 (d)). The latter value has been opportunely increased using a specific coefficient to account for torsional effects. Finally, commercial devices have been selected from the manufacturers’ catalogues. More details about the design choices (i.e. design criteria, device performances and isolation systems configurations) can be found in [Cardone et al., 2019b].

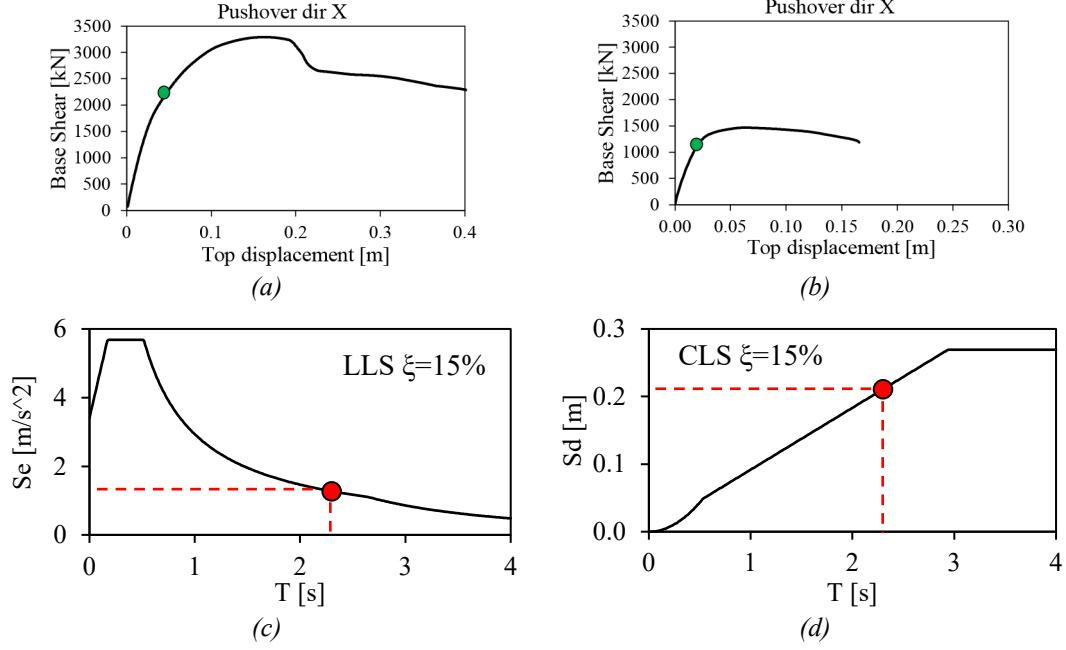


Figure 3. Elastic limit for the (a) AQ_{EX} and (b) NA_{EX} building in the fixed-base configuration and (c-d) Design procedure for the AQ_{EX} building.

For new base-isolated buildings, the design of the isolation system has been performed by linear dynamic analyses, aimed at simultaneously limiting the displacement demand to the superstructure, and ensuring its elastic behaviour at *LLS*. Target fundamental periods ranging from 2.4 s to 3.3 s have been thus derived, for the selected case-study buildings, as illustrated in [Ragni et al., 2018a]. Then, effective periods have been calculated based on the dimensions of isolators, according to indications of the main Italian manufacturers, and on nominal properties of the isolation bearing at the average design shear strain at the *CLS*.

Table 2 summarizes the geometric characteristics and design safety verification outcomes for the rubber-based isolation systems adopted in this study. All the *HDRBs* are characterized by a soft compound (shear modulus G equal to 0.4 MPa) and equivalent viscous damping ratio (ξ) equal to 15%. In Table 2, the devices are identified by a three-number code composed by the nominal diameter (ϕ), the total rubber layer thickness (t_e) and the single rubber layer thickness (t_r). Similarly, the selected *FSBs* are identified by their vertical load capacity (V), displacement capacity ($d_{tot}=d_{tot,x}=d_{tot,y}$, expressed in mm) and pot diameter (Φ_p). The effective fundamental period of the base-isolated building (T_{is}) and the nominal (design) maximum displacement capacity of the devices ($d_{max,HDRB}$ and $d_{max,FSB}$) are also shown. For *HDRBs*, $d_{max,HDRB}$ is the value corre-

sponding to the attainment of a maximum design rubber shear strain equal to 2 (i.e. 200%), according to the explicatory notes of the *NTC2018* [CS.LL.PP. 2019] and the manufacturers' catalogues. For *FSBs*, $d_{max,FSB}$ is conventionally assumed equal to $1.2d_2$, in compliance with [CEN-EN 2005], where d_2 represents the design displacement of the isolation system at the *CLS*. It is worth noting that, the value $1.2d_2$ turns out to be approximately equal to the design displacement capacity of *HDRBs* increased by 50 mm. Finally, in Table 2 the demand/capacity ratios in terms of shear strain (*D/C shear*), compression load (*D/C comp*) and tensile stress (*D/C tens*) are summarized for each case study for the design condition. As can be observed, all the rubber-based isolation systems have been designed using similar *D/C* ratios, very close to 1, in particular for shear and compression.

Adopting a rubber-based isolation system composed by *HDRBs* only, no design solutions was found for the existing building located in Naples (*NA_{EX}*). On the other hand, an isolation system composed by two different typologies of *HDRBs* have been used for the *AQ_{EX}* building (labelled as *HDRB-AQ_{EX}* in Table 2). A design solution has been found for both case-studies using *HDRB+FSB* isolation systems (see Table 2).

More details on the design criteria and results of the design safety verifications can be found in [Ragni et al., 2018a, Cardone et al. 2019b].

Table 2. Geometric characteristics and design safety verification outcomes for the rubber-based isolation systems considered in this study.

Case study	HDRB $\phi/t_e/t_r$	FSB $V/d_{tot}/\phi_p$	d_{max} [mm] HDRBFSB	T_{is} [s]	D/C shear	D/C comp	D/C tens
HDRB-AQ _{EX}	550/154/7+600/152/8	-	300	-	2.49 0.81	0.99	0.79
HDRB+FSB-AQ _{EX}	600/152/8	3500/700/250	300	350	2.68 0.82	0.93	0.14
HDRB+FSB-NA _{EX}	450/102/6	3500/500/250	200	250	3.30 0.89	0.98	0.00
HDRB-AQ _{NEW}	550/154/7+600/150/6	-	300	-	2.46 0.86	0.97	0.33
HDRB-NA _{NEW}	500/126/6+550/126/7	-	250	-	2.52 0.74	0.84	0.00
HDRB+FSB-AQ _{NEW}	600/176/8	3500/800/250	350	400	3.04 0.85	0.98	0.19
HDRB+FSB-NA _{NEW}	500/102/6	3500/500/250	200	250	2.79 0.88	0.79	0.00

Definition of Performance Levels

The seismic performances of the examined case studies have been evaluated considering two specific performance levels, namely the *Global Collapse (GC)* and the *Usability-Preventing Damage (UPD)* performance levels.

The occurrence of the *UPD* has been assessed based on a multi-criteria approach combining the following main concepts: (i) reparability of non-structural elements, (ii) complete protection of structural elements and (iii) no interruption of use of the building towards frequent seismic events. The top displacement threshold associated with the attainment of the *UPD* performance level has been defined, for each case-study, by means of pushover analysis performed on the superstructure in the fixed-base configuration (see Table 3). More details about the mentioned approach are available in the Appendix A of [ReLUIS-RINTC 2018]. As stated in [Ragni et al., 2018a, Cardone et al., 2019b], the isolation system and the superstructure represent two elements of the same in-series system. As a consequence, the *GC* is assumed to occur if either the superstructure or the isolation system fails. For what concerns the superstructure, the collapse is associated with the occurrence of the first of the following conditions [Ricci et al. 2018], (checked on the capacity curve of the building in the fixed-base configuration): (i) 50% decrease of the lateral strength on the pushover curve; (ii) the first column classified as shear-controlled (prior to or after flexural yielding) reaches a chord rotation equal to 0.10, corresponding to the loss of axial load carrying capacity [Ricci et al. 2019]. In other words, superstructure collapse (hence the whole system collapse) occurs when, in one of the two main directions, the

maximum value of the top displacement derived from dynamic analyses reaches the top displacement corresponding to the first of the aforementioned limit conditions (see Table 4). More details can be found in [Ragni et al., 2018a, Cardone et al., 2019b].

Table 3. UPD superstructure limit displacements [mm]

Direction	Existing Buildings		New Buildings			
			HDRB		HDRB+FSB	
	AQ _{EX}	NA _{EX}	AQ _{NEW}	NA _{NEW}	AQ _{NEW}	NA _{NEW}
X	51	37	59	60	59	42
Y	64	49	57	56	66	61

Table 4. GC superstructure limit displacements [mm]

Direction	Existing Buildings		New Buildings			
			HDRB		HDRB+FSB	
	AQ _{EX}	NA _{EX}	AQ _{NEW}	NA _{NEW}	AQ _{NEW}	NA _{NEW}
X	205	170	501	581	488	565
Y	110	130	271	342	267	324

The failure modes considered for HDRBs are cavitation, shear and buckling. The failure criteria assumed to assess the occurrence of cavitation and shear are similar to those proposed in [Ragni et al., 2018a], where the *HDR Bearing Element* was adopted to describe the non-linear cyclic behaviour of *HDRBs*. In particular, the cavitation failure mode of a single bearing is supposed to occur in the post-cavitation branch, for an axial tensile strain equal to 0.5. For the shear failure, a limit shear strain equal to 3.5 has been considered. The global collapse condition (of the whole building due to the isolation system collapse) is conventionally reached when (at least) 50% of the devices of the isolation system simultaneously fail due to cavitation (tension failure mode of the isolation system) or shear (shear failure mode of the isolation system), respectively. It is worth noting that, with regard to the shear failure, the choice of 50% of the total number of devices is merely conventional and on the safety side. In fact, very few experimental evidences are available regarding the redistribution capacity within the isolation system after the failure of a certain number of bearings and on their post-collapse behaviour in shear [Nakazawa et al. 2011]. In the case of tension (associated with the post-cavitation) the choice of 50% is also conventional and on the safety side, because usually only few bearings (under corner columns

or staircases) are subjected to this kind of failure mode. More details about the described assumptions can be found in [Ragni *et al.*, 2018a]. On the other hand, in this paper, the collapse criterion adopted for buckling is different from past studies. As a matter of fact, indeed, in the previous studies (using the *HDR bearing element*), a simplified force-based criterion was adopted in which the P/P_{cr} ratio (i.e. the ratio between the current axial load P and the critical buckling load P_{cr}) was monitored [Ragni *et al.*, 2018]. The buckling collapse of the isolation system was conventionally deemed to occur when at least 50% of the *HDRBs* reached, at the same time, a P/P_{cr} ratio ≥ 1 .

In this study, the collapse criterion associated with buckling has been revised, since *HDRBs* have been modelled with the *Kikuchi Bearing Element*, which explicitly simulate the post-buckling behaviour of *HDRBs*. Consequently, a failure criterion in terms of compressive strain has been adopted. In particular, for any single device, buckling failure mode occurs for an axial compression strain equal to 0.5, even if experimental results showed that rubber bearings can sustain even higher vertical axial deformation after buckling [Monzon *et al.* 2016]. However, mechanisms other than those considered in the building FEM model could take place for very large vertical displacements. Thus, the limit threshold of 0.5 for the compression strain has been prudently assumed for the analysis reliability. Such individual criterion, coupled with the global collapse criterion, i.e. the simultaneous achievement of a compression strain equal to 0.5 for one half (50%) of the devices, appears realistic.

For *HDRB+FSB* isolation systems, two additional failure criteria have been considered for *FSBs*: (i) the attainment of a critical uplift value corresponding to $H/2$, where H is the total height of the device, and (ii) the attainment of a critical value of horizontal displacement corresponding to a limit value of compression stress, equal to 60 MPa according to [prEN 1337-5]. The first criterion ($H/2$) has been set based on the information provided by the main Italian manufacturers. As a matter of fact, indeed, as the horizontal displacement increases, the effective resisting area of the device reduces, and as a consequence the contact pressure increases. Numerical simulations [Cardone *et al.* 2019c] showed that the aforesaid compression rate limit threshold is usually reached for a value of the horizontal displacement approximately equal to

the design displacement capacity of the device ($d_{max,FSB}$) increased by an extra-displacement $\alpha\Phi_p$, with $\alpha \approx 1/2$. All that considered, in this study the ultimate displacement capacity of the $FSBs$ has been conventionally assumed equal to $d_{max,FSB}+1/2\Phi_p$.

The global collapse of an $HDRB+FSB$ isolation system due to $FSBs$ is deemed to occur when the horizontal displacement of the centre of gravity of the isolation floor is equal to the aforesaid limit value or when at least 50% of the devices reach the mentioned uplift threshold.

Failure modes and collapse conditions considered in this study for rubber-based isolated structures are summarized in Table 5.

Table 5. Failure modes and collapse conditions for rubber-based isolated buildings

Failure modes		Collapse conditions
Superstructure	Superstructure collapse	The relative displacement between the top of the building and the isolation level is equal to the lower value between: (i) the top displacement from POA corresponding to a peak strength reduction of 50% on the negative slope and (ii) the top displacement from POA corresponding to the first brittle failure in a structural element
Isolation System	Compression	50% of elastomeric devices reaches an axial compression strain (ϵ_c) greater than or equal to 0.5
	Tension	50% of elastomeric devices reaches an axial tensile strain (ϵ_t) greater than or equal to 0.5
	Shear	50% of elastomeric devices reaches a shear strain (γ_r) greater than or equal to 3.5
	Overstroke and uplift	(i) The horizontal displacement of the center of gravity of the isolation floor is equal to the ultimate displacement capacity or (ii) the 50% of devices reaches the critical uplift value.

Modelling approach

Modelling assumptions

The modelling strategy adopted for both isolation system and superstructure takes into account the most recent progress in the field of nonlinear finite element modelling. In particular, big efforts have been made to represent the complex behaviour of rubber bearings.

The main challenge of a bearing model for a reliability analysis is to reasonably simulate the response under a wide range of seismic input levels, especially beyond the design conditions

1 and up to the collapse of the device. Many aspects of *HDRBs* behaviour should be considered
2 under extreme loadings [Kelly, 1997 and Kumar et al. 2014] such as coupled bidirectional mo-
3 tion in horizontal directions, coupling of vertical and horizontal motion, cavitation and
4 post-cavitation behaviour in tension, strength degradation in cyclic tensile loading due to cavi-
5 tation, variation in critical buckling load capacity due to lateral displacement, post buckling be-
6 haviour, strength degradation in cyclic shear loading due to Mullins effect, shear fracture, post
7 failure behaviour and tension fracture. However, none of the numerical models available in the
8 literature is able to capture all these phenomena at the same time [Grant et al., 2004; Tubaldi et
9 al., 2017; Ragni et al., 2018b, Kumar et al., 2014, Ishii and Kikuchi, 2019], but among them,
10 the latest version of the *Kikuchi Bearing Element* [Ishii and Kikuchi, 2019], recently imple-
11 mented in OpenSees, has been chosen in this work.

12 The *Kikuchi Bearing Element* is a fully 3D model that differently to the others takes into
13 account the coupled behaviour in the vertical and horizontal direction through its large dis-
14 placement formulation. In particular, it is able to capture the well-known geometric nonlinear
15 effect called “*P- Δ* ” effect: the reduction of the horizontal stiffness related to the increase of ver-
16 tical load and horizontal displacement. Such peculiarity appears very important especially for
17 medium-high level of vertical pressure as emerged from the experimental results used for the
18 model calibration within this work [Brandonisio et al. 2017] (see “Model Calibration” section)
19 and also highlighted in other studies, i.e. [Koh and Balendra, 1989].

20 The *Kikuchi Bering Element* is based on the *two-springs model* philosophy, but compris-
21 ing the nonlinear behaviour of the springs and using a different arrangement of them. More in
22 detail, the three-dimensional analytical model features triaxial interaction between the two hori-
23 zontal components, and the vertical component. The shear bidirectional behaviour is based on
24 the use of *Multi Shear Spring model (MSS)* [Wada and Hirose, 1987] while the vertical Euler
25 column buckling behaviour is based on the *Multi Normal Spring model (MNS)*. The arrange-
26 ment of *MSS* and *MNS* is shown in Figure 4. In this way the model incorporates both the influ-
27 ences of material and the geometrical nonlinearities.

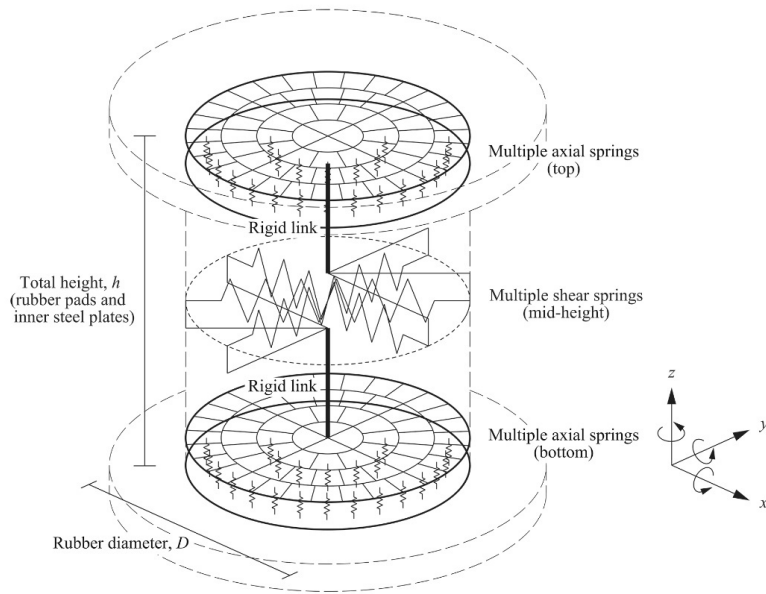


Figure 4. Multi spring mechanical model for circular elastomeric bearing (from Ishii and Kikuchi 2019).

Thus, the model is able to properly predict the behaviour in the post-buckled condition even for squared bearings and variable vertical load due to the rocking motion of the superstructure during an earthquake. This is an essential feature for reliability analysis because the actual hysteresis behaviour of isolation bearings under a structure subjected to severe earthquake shaking is not the same as that obtained from cyclic shear tests of a bearing with constant axial stress, because of the influence of the variation of vertical load due to overturning forces. In particular, external bearings may show a strongly asymmetric hysteretic cycle with a substantial pure shear behaviour for one side of the cycle (lowest compression) and a possible post-buckled behaviour in the other side (higher compression) [Kikuchi et al., 2010, Takaoka et al. 2011].

For the *Multi Shear Spring (MSS) model*, the *KikuchiAikenHDR* material has been used. The original version implemented in Opensees features only a limited set of pre-calibrated rubber compounds, but they can be slightly adjusted to better fit a specific rubber compound using three correction coefficients controlling the equivalent shear modulus (c_g), the equivalent viscous damping ratio (c_h) and the ratio of shear force at zero displacement (c_u), respectively. Being based on a limited number of parameters, the calibration process of such model appears simple. On the other hand, for the same reason, important phenomena, such as stiffening for

high shear deformation and scragging, are neglected. As a consequence, in this work, the shear behaviour of HDRBs has been calibrated with reference to a specific cycle (i.e. the third cycle, according to [EN15129, 2009]) under the hypothesis that the behaviour in the virgin state [Tibaldi et al 2017, Ragni et al 2018b] is not significant towards the final performance assessment.

For the *Multi Normal Spring (MNS) model*, the *AxialSP* material, already implemented in the OpenSees material library, has been used. Such material is fully defined by the following parameters and consequently not calibrated: (i) initial elastic vertical stiffness E_{init} , (ii) post elastic stiffness in tension ($1/100E_{init}$) and compression ($1/2E_{init}$), (iii) cavitation stress and (iv) compression yielding stress. According to [Ishii and Kikuchi, 2019] the following relationship can be used to derive the elastic E_{init} :

$$E_{init} = K_{bulk} \left\{ 1 - \frac{2}{\bar{\lambda}} \frac{I_1(\bar{\lambda})}{I_0(\bar{\lambda})} \right\} \quad (1)$$

where K_{bulk} is the bulk modulus of the rubber compound, usually equal to 2000MPa, I_1 and I_0 are the modified Bessel function of the first kind of order 1 and 0 respectively whereas $\bar{\lambda}$ is the dimensionless parameter

$$\bar{\lambda} = \frac{D}{t} \sqrt{\frac{3G}{K_{bulk}}} \quad (2)$$

Moreover, values equal to 1MPa and -100MPa are usually adopted for cavitation stress and compression yielding stress, respectively [Ishii and Kikuchi 2019]. Comparing the numerical results obtained adopting the mentioned values of the model parameters with those derived by several calibration tests performed within this work on common rubber devices generally used in the Italian context, a sensible overestimation of the “*P-Δ*” effects has been observed. The key point of the different ability to predict the post-buckling behaviour can be found in the hidden hypothesis that is at the base of this model: the behaviour of the single normal spring in tension, representing a single fiber, is the same of the whole bearing. This hypothesis could be true depending on the isolator geometry. As a matter of fact, for isolators with very large primary shape factors and conventional values of the secondary shape factors (e.g., $S_1=30$ and $S_2=3$),

the compression buckling could be triggered by the cavitation of the perimetral fibers subjected to tension. Differently, slender bearings with lower primary shape factors and larger secondary shape factors could experience buckling before the local cavitation of the rubber. The primary shape factor of the rubber bearings examined in this work is around 20, lower than that of the bearings tested within [Yamamoto 2009, Kikuchi et al. 2010 Ishii and Kikuchi 2019] that are higher than 30. Thus, to avoid the local cavitation of the bearing before the buckling, the material used for the *MNSs* has been replaced by a simple elastic material with stiffness equal to E_{init} . Obviously, in the described condition, the model is not able to capture the nonlinear axial behaviour associated with cavitation. As a consequence, the *Kikuchi Bearing Element* has been implemented in the building model in-series with a rigid plastic spring describing the global cavitation of the rubber. The external spring is characterized by a rigid behaviour under compression and in the range of tension forces lower than the cavitation threshold, while it is properly calibrated to describe the inelastic post-cavitation behaviour above the mentioned threshold (see Figure 5). In particular, as the *AxialSP* material does not feature any cyclic degradation of the post-cavitation behaviour, median values of the post-cavitation stiffness and force threshold have been adopted in the model (similar to the third-cycle concept used for the shear behaviour), leading to a cavitation force of $2GA$ and a post-cavitation stiffness equal to $0.43\% E_{init}$, based on experimental result of [Warn 2006]. In this way, the global building model is able to capture the influence of cavitation on the rocking motion during an earthquake.

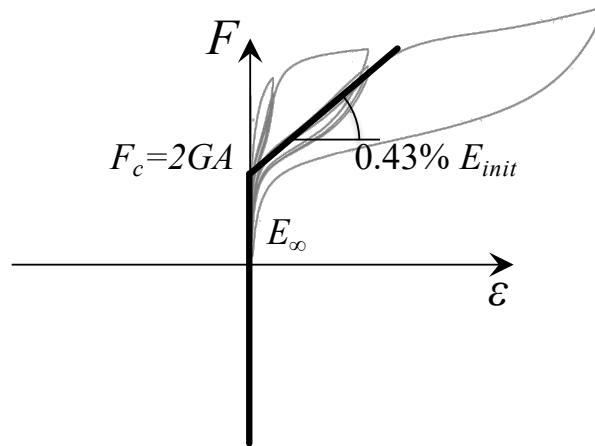
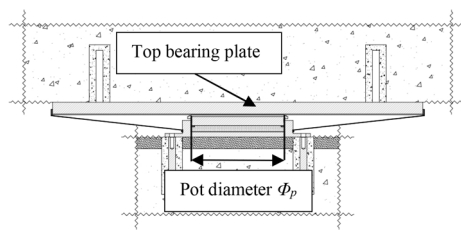


Figure 5. Uniaxial constitutive model of the vertical in-series rigid-plastic spring for cavitation behaviour (superimposed on test from Warn 2006).

As far as the modeling of flat sliding bearings is concerned, the element flatSliderBearing has been used adopting a velocity-dependent and axial-load-dependent friction model [Constantinou et al., 1990], and assuming a friction coefficient at the maximum load capacity equal to 1% for fast velocities and 0.5% for low velocities, based on the results of manufacturer's type tests. More details about slider modeling can be found in [Cardone et al., 2019a].

It is worth noting that such low damping coefficients implies a negligible effect of the sliders on the isolation system behaviour (i.e. extra-damping). This must be assessed by suitable acceptance tests on materials or devices.



\mathbf{a}_{Slow}	constant for coefficient of friction at low velocity	0.02073
\mathbf{n}_{Slow}	exponent for coefficient of friction at low velocity	0.9
\mathbf{a}_{Fast}	constant for coefficient of friction at high velocity	0.04146
\mathbf{n}_{Fast}	exponent for coefficient of friction at high velocity	0.9
\mathbf{a}_0	constant rate parameter coefficient	0.00458
\mathbf{a}_1	linear rate parameter coefficient	0
\mathbf{a}_2	quadratic rate parameter coefficient	0

Figure 6. FSB device and model parameters

Model calibration

The results of an experimental campaign [Brandonisio et al 2017] performed at the SisLab (Materials and Structures Test Laboratory) of the University of Basilicata on three circular HDRBs, have been used for the model calibration of the rubber bearings. The main characteristics of the tested bearings are reported in Table 6. As can be seen, the mentioned bearings feature different geometrical dimensions but the same soft rubber compound (labelled as S - Soft), characterized by nominal values of shear stiffness G and damping factor ζ equal to 0.4MPa and 15% respectively. In Table 6, Φ denotes the outer rubber diameter, Φ' the inner steel shim diameter, t_r the single rubber layer thickness, t_e the total rubber layer thickness, S_1 the primary shape factor ($S_1=\Phi'/4t_r$) and S_2 the secondary shape factor ($S_2=\Phi'/t_e$).

Table 6 Geometrical characteristics of the tested HDRBs

HDRB code	Φ	Φ'	t_r	t_e	S_1	S_2
	[mm]	[mm]	[mm]	[mm]		
SI-S-500-176	500	490	5.5	176	22.7	2.8
SI-S-600-217	600	590	7	217	21.4	2.8
SI-S-700-207	700	690	9	207	19.5	3.4

More in detail, a specific sequence of tests has been performed on each device. First of all, the static compression stiffness test (*Axial Test*, test 1-2) and horizontal *Shear Cyclic Test* (*SCT*, test 3) have been carried out. Then, a series of *Shear Quasi static Test* (*SQT*), alternated with the repetition of the *SCT* (tests 6 and 16), have been conducted (Figure 7). The *SQTs* are half cycle (positive shear deformation only) tests, organized in groups of three with the same maximum shear displacement and increasing vertical compression (6 MPa, 10 MPa and 14 MPa). Some special tests have been also performed to better assess extreme conditions. More details can be found in [Brandonisio et al. 2017]. It should be noted that the whole test sequence has been performed on a same device, thus results are strongly affected by the load history dependent behaviour of the rubber effect, in the case of multiple repeated cycles [Mullins, 1969, Tubaldi et al. 2017 and Ragni et al. 2018b].

Among the three sets of tests, those carried out on the SI-S 700-207 have been chosen to calibrate the numerical model because it is the most complete series. The other two sets (tests on SI-S 500-176 and SI-S 600-217) have been used to verify the ability of the calibrated model to reproduce the experimental results.

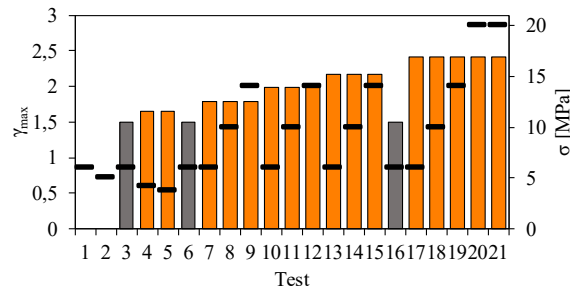


Figure 7. SI-S 700-207 test sequence (grey bars refer to strain amplitude of SCTs, orange bars refer to strain amplitude of SQTs, while horizontal dashes represent the vertical compression stress)

More in detail, the rubber compound material used for the isolators model is the X0.4-0MPa [Bridgestone Corporation, 2017] with a shear modulus equal to $G=0.4$ MPa and a

bulk modulus equal to $K_{bulk}=2000\text{MPa}$. Figure 8 shows results of the first two axial tests which are properly predicted by the model. Obviously, as the vertical spring doesn't feature any viscous component, it is not able to predict the unloading branch. However, such limitation is not crucial during a seismic event as the vertical load variation is a dynamic action.

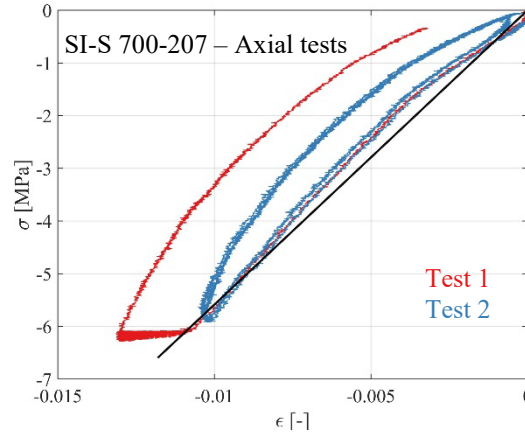


Figure 8. Comparison of axial test experimental results and calibrated model for SI S 700 207 HDRB

As far as the shear cyclic behaviour is concerned, values equal to 1.15, 0.75 and 0.75 have been adopted for the correction coefficients c_g , c_h and c_u , respectively, to fit the third cycle (according to [EN15129, 2009]) of the first *SCT* (i.e. test 3 of Figure 9). To predict the hysteretic response of the subsequent *SCTs* (test 6 and 16 in Figure 9), c_g has been further corrected (as percentage k of the initial value) to reproduce the scragging effects due to previous test. It should be noted that the reduction percentage calibrated based on Test 6 and 16 is taken constant in simulating the *SQTs* following each *SCT*. Moreover, it is worth noting that the same reduction percentage has been applied to the axial springs of the model to simulate *SQTs*, even if further investigation would be needed on the influence of repeated shear tests on the axial properties of the device.

Figure 9(a) compares the results of the three *SCTs* (Test 3, 6 and 16) in order to highlight the stress softening due to the load history dependence. The half cycles of the *SQTs* performed between the *SCTs* influence only the positive range of shear deformation, confirming the deformation-induced anisotropy of the material [Tubaldi et al 2017, Ragni et al 2018b]. Figure 9 (b)-(c)-(d) show a very good agreement between the experimental and the numerical results rel-

evant to the *SCTs*. Obviously, the model cannot predict the first loading branch of the *SQTs*, being the model calibrated on the third cycle, nor the model can follow the asymmetrical behaviour of the rubber. The simulation of the *SQTs* are reported in Figure 10, which confirms the ability of the model to also simulate the device response under large displacements and large axial loads.

It worth to note that the stiffness percentage reduction has been used only to simulate the experimental tests, while unadjusted values are used in the multi-stripe analyses because several repeated cycles on a same device are not representative of an earthquake scenario. More details regarding the model calibration can be found in [Micozzi 2020].

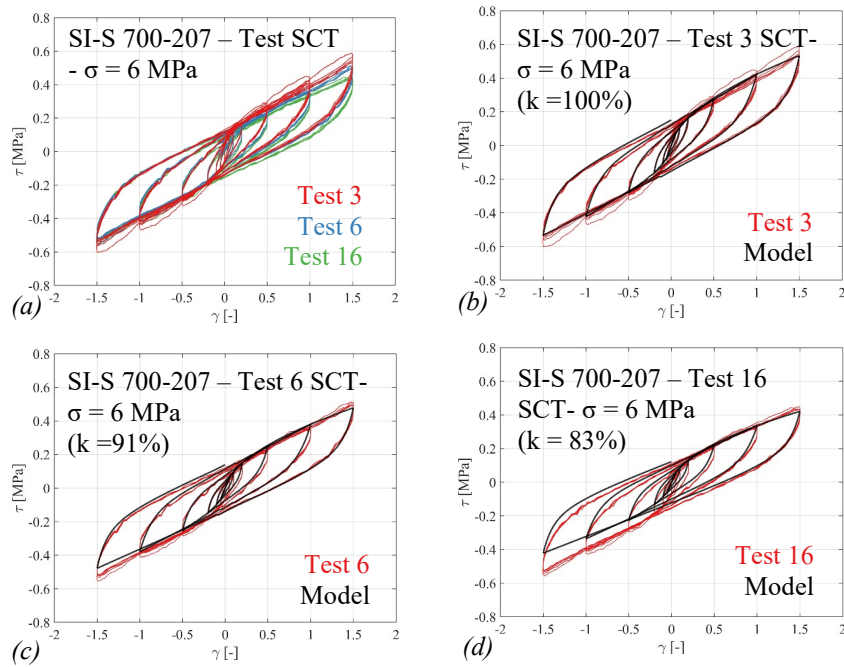


Figure 9. Superimposed *SQTs* for SI-S 700-207 HDRB and comparison between experimental results and calibrated model.

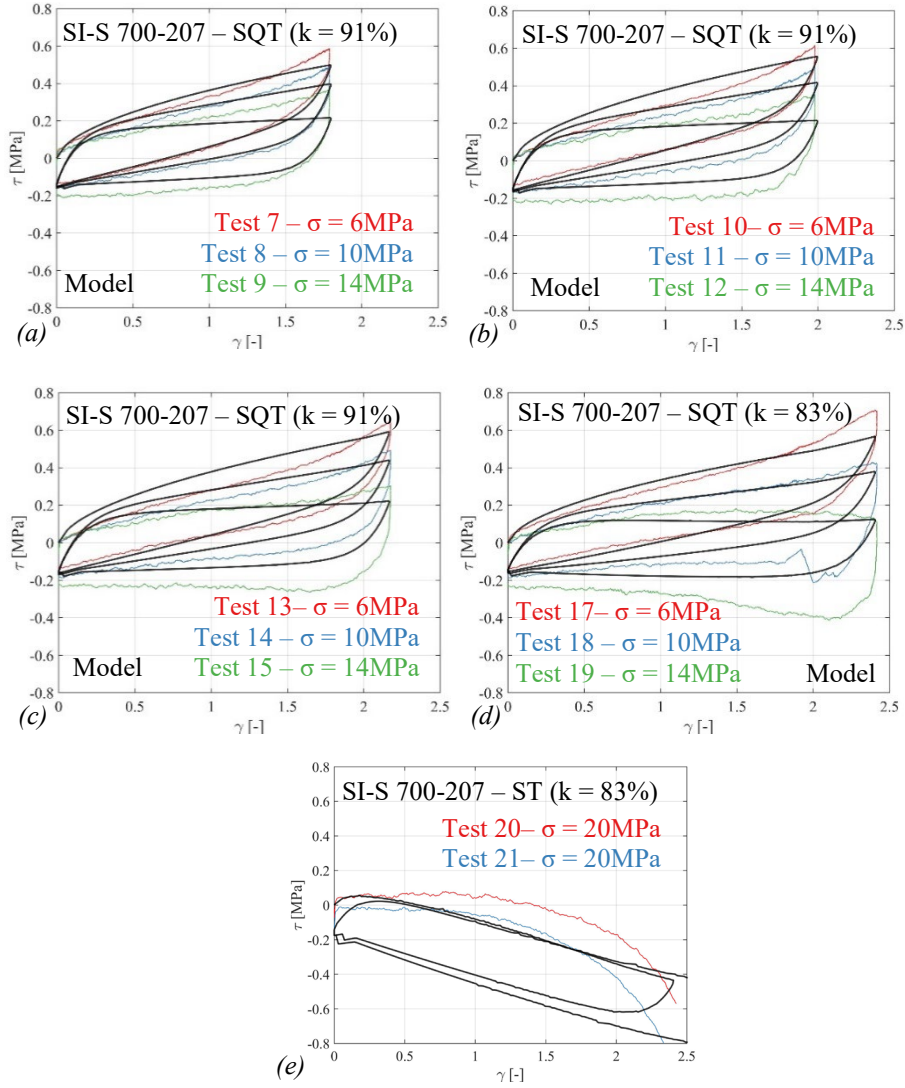


Figure 10. Comparison between SQT experimental results and calibrated model for SI-S 700-207 HDRB

As far as the superstructure is concerned, pragmatic choices have been done in order to limit the computational efforts, maintaining as much as possible the most reliable and advanced features of the current state-of-the-art. In particular, a lumped plasticity model has been chosen for beam and column elements of the superstructure, whereas elastic beams have been used for the base floor grid above the isolation system. The choice of representing the superstructure with a nonlinear model is justified by the results of recent studies on this topic [Cardone *et al.*, 2013, Cardone and Flora, 2016], which pointed out the effects of the inelastic behaviour of the

1 superstructure on the seismic response of base isolated buildings. The model also includes the
2 staircase structure (inclined beams and cantilever steps) as well as masonry infill panels.

3 Regarding the RC members, in particular, the model selected for the description of the
4 section flexural behaviour is the well-known model by Ibarra [Ibarra and Krawinkler, 2005, Ibarra
5 et al., 2005], implemented in OpenSees as *modIMKmodel*. To consider shear failures before
6 or after flexural yielding in beam/column elements and in beam column joints, all the hinges
7 have been pre-qualified either as (i) *ductile*, in which the shear failure is avoided and the
8 moment-rotational backbone model is not modified, or (ii) *shear critical*, in which the backbone
9 is reduced after the shear failure, following a softening branch up to zero based on the empirical
10 proposal by [Aslani and Miranda, 2005]. More details about this collapse criterion can be found
11 in Ricci et al. 2019. In the (ii) case, if the shear failure occurs before yielding the element is defined
12 as “brittle”, whereas if shear failure occurs between yielding and the ultimate bending
13 moment the element is characterized by a flexure-shear interaction failure mechanism. Regarding
14 the beam-column joint, the joint panel model called “*scissors model*” has been used. It is a
15 very simple and computationally efficient joint model, but also sufficiently accurate in predicting
16 the experimental beam-column joint panel behaviour for simulating the seismic response of
17 non-ductile RC frames [De Risi et al., 2017]. The adopted constitutive model accounts for two
18 possible failure mode of the beam-column joints: joint shear failure prior to or after the
19 achievement of yielding of the adjacent beams/columns (in strong column - weak beam or weak
20 column-strong beam hypothesis).

21 The contribution of masonry infills is modelled with an equivalent compression-only
22 strut. The skeleton curve of the diagonal strut has been derived according to a modified version
23 of the *Decanini model* [Sassun et al., 2016]. The effects of the openings have been taken into
24 account through suitable reduction factors [Decanini et al., 2014].

25 More information on the superstructure modelling can be found in [Camata et al, 2017,
26 Ricci et al., 2018, Ricci et al. 2019].

27

28

Non-Linear Time History Analysis (NTHA)

Seismic Input

Multi-Stripe non-linear dynamic analyses (*NTHA*) have been performed to evaluate the seismic performances of the examined case-studies towards *GC* and *UPD* performance levels. As mentioned before, 10 earthquake intensity (*IM*) levels have been investigated. Considering that the fundamental periods of the examined case-studies range from 2.5 to 3.3 s, a unique conditioning period (T^*) equal to 3.0 s has been assumed for the seismic performance assessment. The values of $S_a(T^*)$ for each *IM* level and for the two considered sites (expressed in terms of geometric mean) are summarized in Table 7. Each “stripe” of seismic response has been then analysed running a set of 20 ground motion pairs featuring the mentioned conditioning period. It is worth noting that, according to Italian Seismic Code (NTC2018), the *IM* associated with level 2 and 6 (labelled as *IM2* and *IM6* in what follows) correspond to the earthquake intensity levels for the verification of the *Damage* and *Collapse Limit States*, respectively.

For the *GC* performance level, the analyses results are provided in terms of number of failures as a function of the *IM* level. More in detail, the total number of records causing a collapse condition for the examined case-study is reported as a function of the *IM* level. Moreover, using different colours, information about the specific failure mode causing collapse (the first one occurring during the analysis) is provided for each *IM* level. On the other hand, for the *UPD* performance level, diagrams summarizing the demand-capacity ratios (D/C) associated with each ground motion pair, as a function of the earthquake intensity level, are presented (for each direction). In particular, the capacity (C) is obtained as described before (see “Definition of Performance Levels” section), while, the demand (D) is represented by the maximum top displacement of the superstructure (with respect to the isolation system) derived from *NTHA* (see Table 3).

It is worth noting that, when the isolation system collapse anticipates the occurrence of the maximum top displacement registered during the analysis, the top displacement associated

with collapse has been assumed as displacement demand (D) in the calculation of the D/C ratio at the UPD performance level. For each IM level, the total number of records leading to a “failure condition” in terms of UPD (conventionally reached for D/C ratios larger than 1) is also provided.

Table 7. Spectral accelerations $Sa(T^*=3s)$, expressed in unit of g, for each earthquake intensity level

IM RP (years)	1 10	2 50	3 100	4 250	5 500	6 1000	7 2500	8 5000	9 10000	10 100000
L'Aquila	0.0002	0.011	0.031	0.062	0.11	0.177	0.271	0.384	0.576	1.053
Naples	0.001	0.009	0.026	0.044	0.067	0.093	0.126	0.162	0.216	0.348

NTHA results for new buildings

Figure 11 (a) and Figure 13 (a) show the results relevant to the GC performance level for the new buildings equipped with HDRBs only, located in L'Aquila and Naples, respectively (i.e. HDRB-AQ_{NEW} and HDRB-NA_{NEW}). As can be seen, results registered for HDRB-AQ_{NEW} (see Figure 11(a)) show no failures at IM levels from 1 to 5. Two failures occur at $IM6$. Then, the number of failures rapidly increases reaching 20 at $IM9$. The shear failure emerged as the prevalent failure mode. The collapse of the superstructure occurs as first failure mode only in a few cases. Such result is directly related to the main peculiarities of the numerical model used to simulate the $HDRBs$ behaviour. In fact, the large displacements formulation of the *Kikuchi Bearing Element* produces a progressive reduction of the horizontal stiffness of the device, which leads to an increase of the horizontal displacements, but generally also a reduction of the shear force transmitted to the superstructure.

As the value of 3.5 for the ultimate shear strain of $HDRBs$ is somehow a safety-side choice (for example, in [Nishi et al., 2019] most of the bearings show shear rupture for strain higher than 4.0), a second shear deformation limit of 4 is also examined to better quantify how this limit affects the final results. The results considering a shear strain limit equal to 4 are shown in Figure 11(b). The total number of failures decreases at $IM6$ (-1), $IM7$ (-2) and $IM9$ (-2), while remaining the same for the other IM levels. Moreover, in many cases, the occurrence of a shear failure,

associated with the revised threshold, is anticipated by the superstructure collapse. As a consequence, overall the assumption on the ultimate rubber shear strain little affects the final results (as shown later in Figure 26).

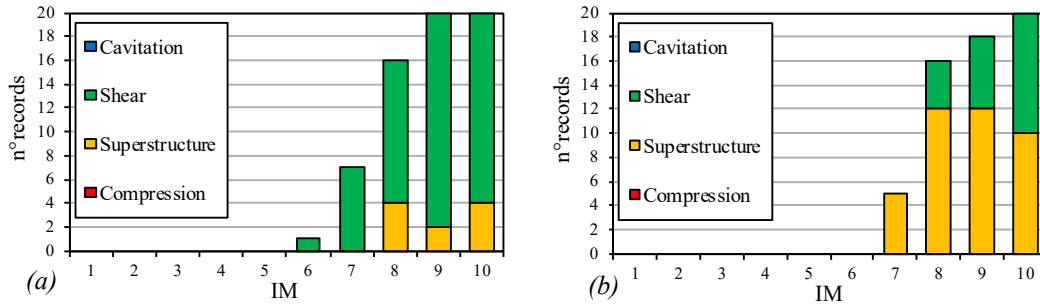


Figure 11. GC results for HDRB-AQ_{NEW}: (a) shear limit 3.5, (b) shear limit 4.0

To better understand the behaviour of the new *Kikuchi Bearing Element* used, Figure 12 shows the vertical and horizontal strain-stress cycles for a corner bearing during a IM9 earthquake. The HDR Bearing Element results of the past research is also showed for comparison purpose.

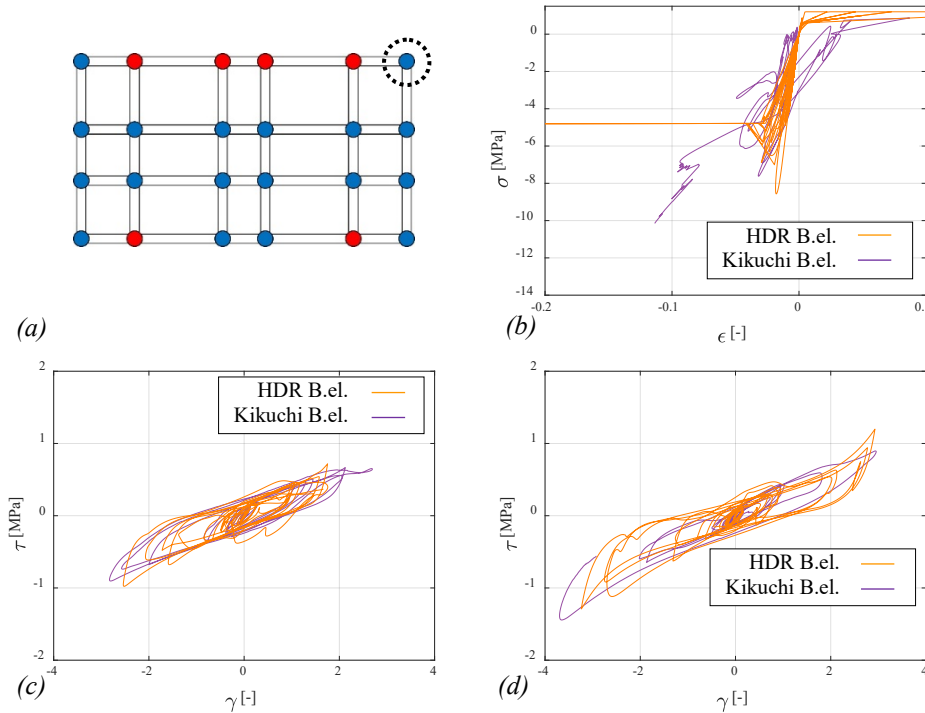


Figure 12. (a) Bearing position, (b) vertical and (c)(d) horizontal hysteresis cycles comparison for HDR Bearing element and Kikuchi Bearing element of the HDRB-AQ_{NEW} case study for a IM9 earthquake

The previous figure highlights the differences between the two models. In particular, the HDR Bearing Element is able to capture the first cycle stiffness and the softening behaviour due to

repeated cycles, while the *Kikuchi Bearing Element* is calibrated on the third cycle because it is not suitable to model the scragging behaviour. Moreover, the *HDR Bearing Element* shows remarkable hardening behaviour at large strains, which does not take place with the *Kikuchi Bearing Element* due to the $P-\Delta$ effects. Finally, it can be observed that the *Kikuchi* hysteresis cycle does not show to a real buckling condition (i.e. the secant stiffness of the loading curve is always positive), but the lower stiffness usually leads to larger displacements. The vertical behaviour is also quite different. In this case, both the models account for the reduction of the vertical stiffness for increasing horizontal displacements, but *HDR Bearing Element* recognise buckling of the bearing (zero tangent stiffness in compression) while *Kikuchi Bearing Element* correctly predict only a vertical stiffness reduction, without a real buckling reached (no vertical or horizontal zero stiffness). The final result is a more realistic prediction of the isolation response for *Kikuchi Bearing Element*. More details can be found in [Micozzi 2020].

Differently, no failures have been registered at *IM* levels from 1 to 9 for *HDRB-NA_{NEW}* (see Figure 13(a)). On the contrary, 18 failures (17 shear failures and 1 superstructure collapse) can be observed at *IM10*. It should be observed that the isolation systems of the two examined cases (*HDRB-AQ_{NEW}* and *HDRB-NA_{NEW}*) have been designed with the same margins towards the limit conditions associated to the Seismic Code prescriptions (see Table 2). Thus, the differences in terms of failure rates are mainly related to the different trends of the seismic hazard of the examined sites, in particular for seismic intensity levels larger than *IM6* (see Figure 27). Finally, similarly to the case-study building located in L'Aquila, the results for *HDRB-NA_{NEW}* have been re-processed considering a shear threshold equal to 4.0 (see Figure 13 (b)) obtaining a reduction of the total number of failures at *IM10* (-4) but a significant increase of the number of cases of superstructure collapse (+6).

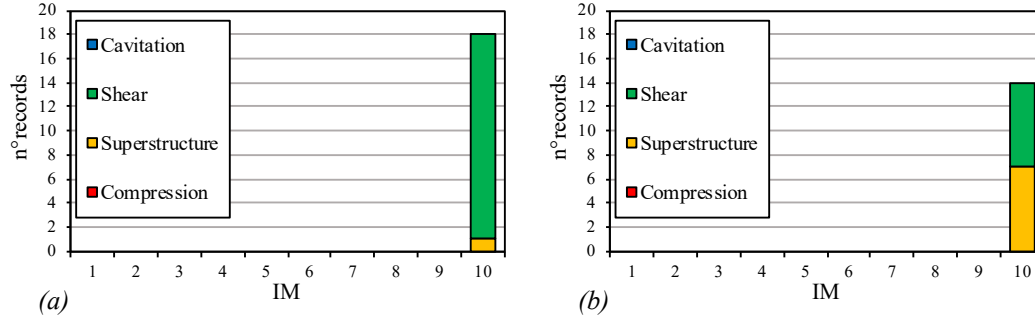


Figure 13. GC results for HDRB- NA_{NEW} : (a) shear limit 3.5, (b) shear limit 4.0

The results relevant to the GC performance level for new buildings equipped with HDRB+FSB isolation system are shown in Figure 14(a) and Figure 15(a). In both cases, no collapses are registered until IM7. However, while for HDRB+FSB- NA_{NEW} only one failure is registered at IM7 and IM8, for HDRB+FSB- AQ_{NEW} the total number of failures is already significant at IM7 (11), reaching 20 at IM9 and IM10. In both the cases, the isolation system collapse represents the prevalent collapse condition. However, while the attainment of the ultimate displacement of the sliders is the dominant failure mode for HDRB+FSB- AQ_{NEW} , the shear failure of HDRB is the dominant failure mode for HDRB+FSB- NA_{NEW} . This result can be ascribed to the ultimate displacement capacity of FSBs assumed for the two models respect to the HDRBs capacity. As done for HDRBs, two different allowable extra-stroke displacement are considered for FSBs, equal to $\alpha=1/2$ and $\alpha=2/3$ the slider diameter, corresponding to a limit contact pressure in the PTFE pads of around 60 MPa and 80 MPa, respectively. Results with these two different thresholds are shown in Figure 14 (a) and (b). For HDRB+FSB- AQ_{NEW} , the ultimate displacement capacity of FSBs turns out to be always lower than HDRBs while the contrary holds for HDRB+FSB- NA_{NEW} (see Table 8), although the design criteria are the same. The difference is the design safety margin towards shear failure of the commercial devices selected for the two cases (see Table 2). It is then clear that, for HDRB+FSB- AQ_{NEW} , even modifying the conventional failure criterion for FSBs (which is associated with the attainment of a critical contact pressure in the PTFE pads), the results in terms of total number of collapses are almost the same and the differences in terms of failure mode are marginal (see Figure 14). On the other hand, for

1 $HDRB+FSB-NA_{NEW}$, the ultimate displacement capacity of FSBs does not affect the results at all
2 (see Figure 15).

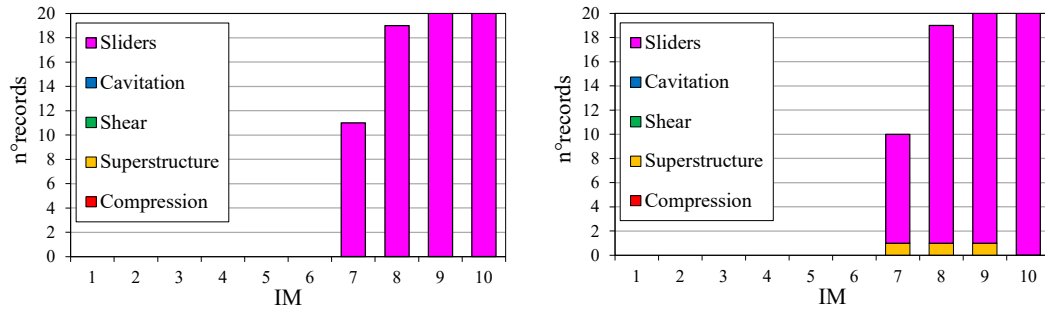


Figure 14. GC results for $HDRB+FSB-AQ_{NEW}$: (a) $\alpha=1/2$, (b) $\alpha=2/3$

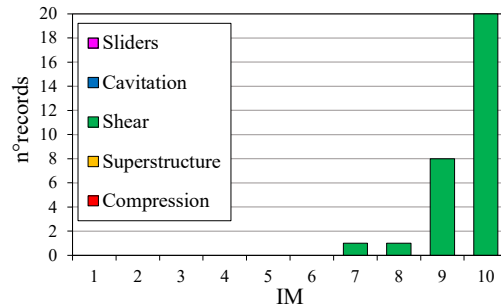


Figure 15 GC results for $HDRB+FSB-NA_{NEW}$ ($\alpha=1/2$)

Table 8. Ultimate displacement capacity of HDRBs and FSBs (mm units) for each case study with $HDRB+FSB$ isolation system

Case study	HDRB	FSB	
		$\alpha=1/2$	$\alpha=2/3$
$HDRB+FSB-AQ_{EX}$	532	475	517
$HDRB+FSB-NA_{EX}$	357	375	417
$HDRB+FSB-AQ_{NEW}$	616	525	567
$HDRB+FSB-NA_{NEW}$	357	375	417

The results in terms of UPD performance level are reported in Figure 16 to Figure 19. For each IM , the D/C values registered during the analysis are provided. Moreover, the total number of failures ($D/C \geq 1$) is reported on the top of the diagrams. It is worth noting that, if the collapse of the isolation system is registered, also UPD is considered attained, whichever is the D/C ratio (spot highlighted with black X). As can be seen, no failures are registered until $IM4$ for the case-studies located in L'Aquila ($HDRB-AQ_{NEW}$ and $HDRB+FSB-AQ_{NEW}$), see Figure 16

and Figure 18, respectively. In particular, D/C values of the order of 0.2 (on average, considering both directions) are obtained at $IM2$, representing the earthquake intensity level associated with the verification of the *Damage Limit State*, according to NTC2018. The different seismic hazard of the two sites significantly affects the results moving the first failures at $IM7$ for the case studies located in Naples ($HDRB-NA_{NEW}$ and $HDRB+FSB-NA_{NEW}$), see Figure 17 and Figure 19. Obviously, as observed for the previous case-studies, the D/C values registered at $IM2$ are much lower than 1, being of the order of 0.15 (on average, considering both directions).

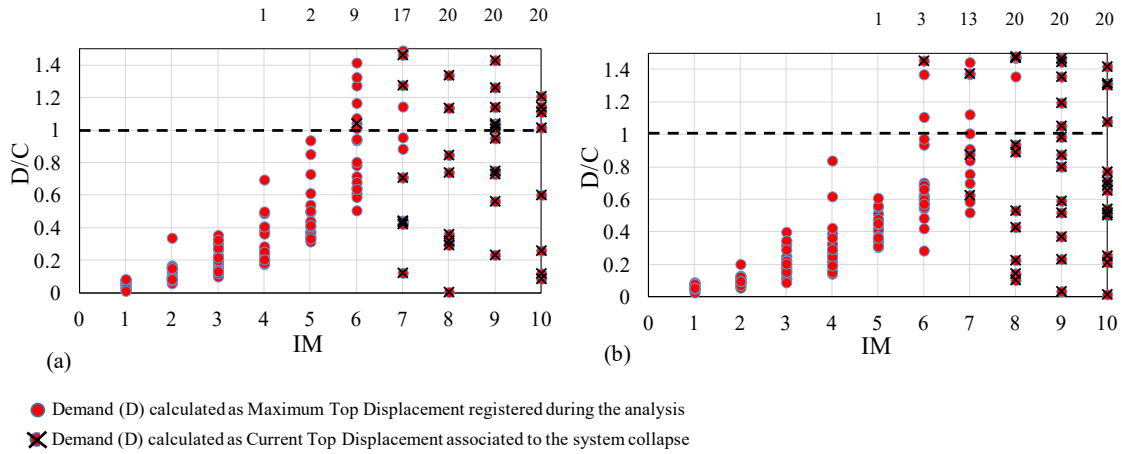


Figure 16. Displacement D/C ratio of the superstructure (UPD) for $HDRB-AQ_{NEW}$: (a) X direction and (b) Y direction.

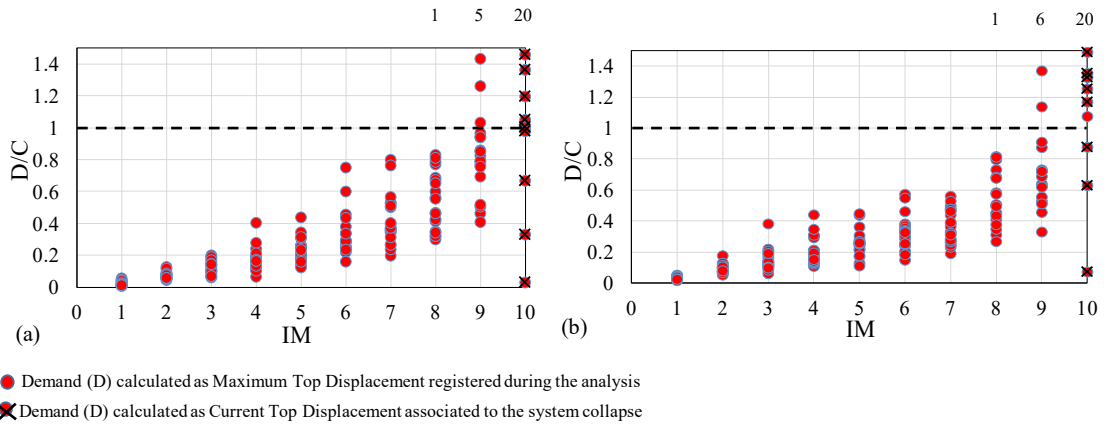
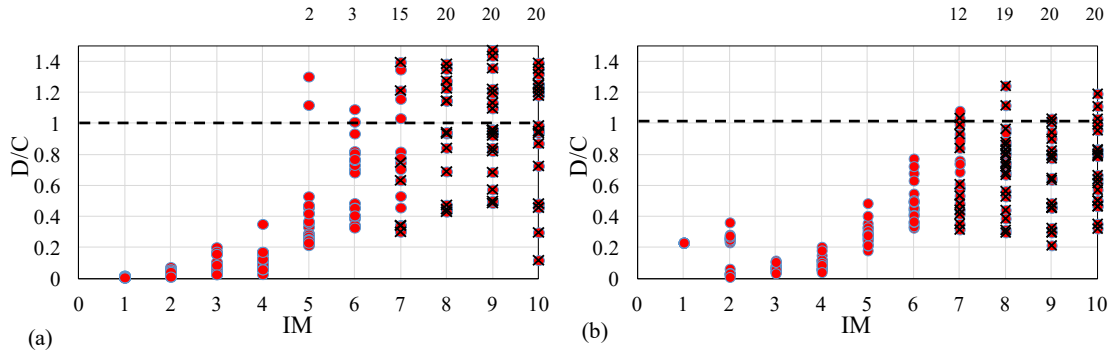


Figure 17. Displacement D/C ratio of the superstructure (UPD) for $HDRB-NA_{NEW}$: (a) X direction and (b) Y direction.

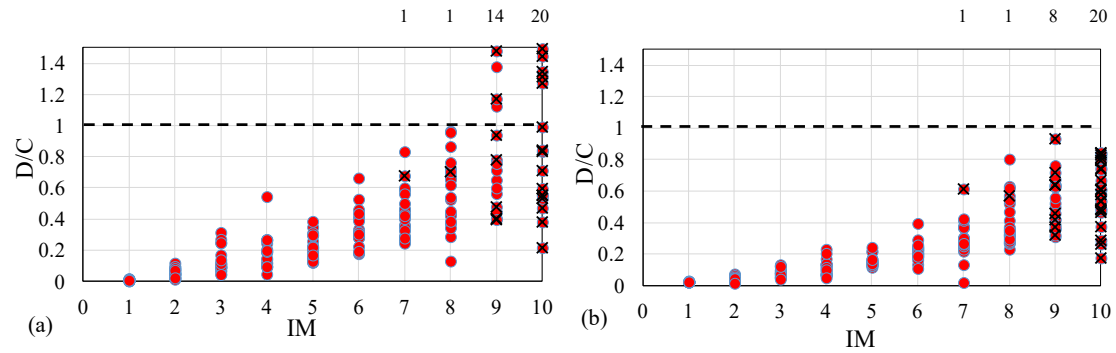
Definitely, large safety margins towards the UPD performance level are observed for all the examined case studies of new base-isolated buildings with rubber isolators, thus confirming the main outcomes presented in [Ragni et al., 2018a] where the same isolation systems were modelled using the *HDR Bearing Element*. In other words, the modelling assumptions (*Kikuchi*

Bearing Element instead of HDR Bearing element) seem to produce limited consequences on the results, in the range of low-to-medium horizontal displacements. Results concerning the GC performance level are also little affected in terms of number of collapses, although the collapse modes considerably change.



● Demand (D) calculated as Maximum Top Displacement registered during the analysis
 ✕ Demand (D) calculated as Current Top Displacement associated to the system collapse

Figure 18. Displacement D/C ratio of the superstructure (UPD) for HDRB+FSB-AQ_{NEW}: (a) X direction and (b) Y direction.



● Demand (D) calculated as Maximum Top Displacement registered during the analysis
 ✕ Demand (D) calculated as Current Top Displacement associated to the system collapse

Figure 19. Displacement D/C ratio of the superstructure (UPD) for HDRB+FSB-NA_{NEW}: (a) X direction and (b) Y direction.

NTHA results for existing buildings

As mentioned before (see “Case studies” section), using HDRBs only no solution are found for the retrofit of the existing building located in Naples, due to the very low shear force capacity of the superstructure. As a consequence, a single case-study building with HDRBs only (i.e. HDRB-AQ_{EX}) has been investigated.

Generally speaking, a limited number of failures is observed at $IM6$ for all the examined case-studies (see Figure 20, Figure 21(a) and Figure 22), while such number becomes significant starting from $IM7$. Considering that the superstructure geometrical characteristics (number of floors, spans and plan layout) and the isolation system configuration of the new buildings (i.e. $HDRB-AQ_{NEW}$, $HDRB+FSB-AQ_{NEW}$ and $HDRB+FSB-NA_{NEW}$) are equal to those of the corresponding existing building retrofitted with rubber-based isolation systems (i.e. $HDRB-AQ_{EX}$, $HDRB+FSB-AQ_{EX}$ and $HDRB+FSB-NA_{EX}$), a comparison in terms of total number of collapses and failure modes is appropriate. First of all, the total number of collapses sensibly increases passing from new to existing buildings, especially at $IM6$ and $IM7$. Moreover, as expected, a considerable increase of the number of cases with superstructure collapse are observed, for each IM . This is mainly ascribed to the lower ultimate displacement capacity of the existing buildings (see Table 4), due to lower ductility capacity of the RC frames and premature shear failure of some RC members. As a consequence, lower safety margin towards the global collapse of the superstructure are obtained for existing buildings, compared to new buildings.

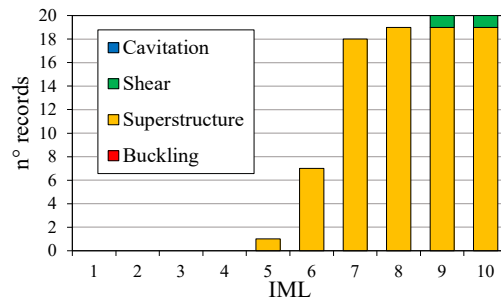


Figure 20. GC results for $HDRB-AQ_{EX}$

Further specific considerations must be done for the $HDRB+FSB$ case studies. Indeed, assuming an extra-stroke equal to 1/2 the slider diameter for $HDRB+FSB-AQ_{EX}$ ($\alpha=1/2$ in Figure 21(a)), the collapse of sliders is still the dominant (first occurring) failure mode. Passing from $\alpha=1/2$ to $\alpha=2/3$ (see Figure 21(b)), the number of cases in which the superstructure collapse is the first occurring failure mode increases, although the total number of collapses remains substantially the same.

Figure 22 shows the results for $HDRB+FSB-NA_{EX}$ case-study. The collapse of the superstructure

remains the dominant failure mode. For what concerns the isolation systems, however, like for $HDRB+FSB-NA_{NEW}$, the shear failure of $HDRBs$ always anticipates the slider failure (see Table 8).

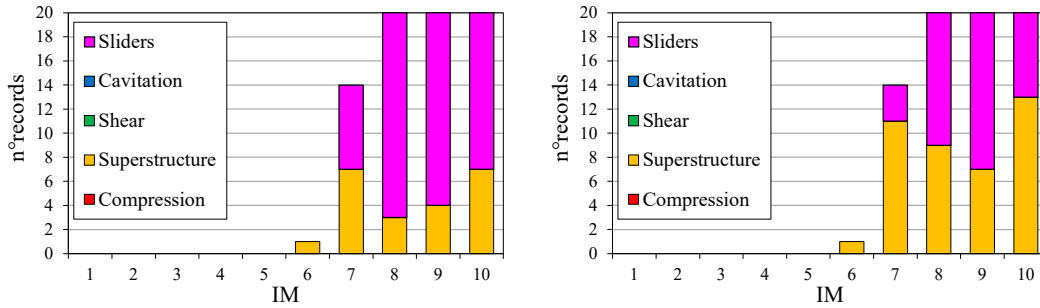


Figure 21. GC results for $HDRB+FSB-AQ_{EX}$ (a) $\alpha=1/2$ and (b) $\alpha=2/3$.

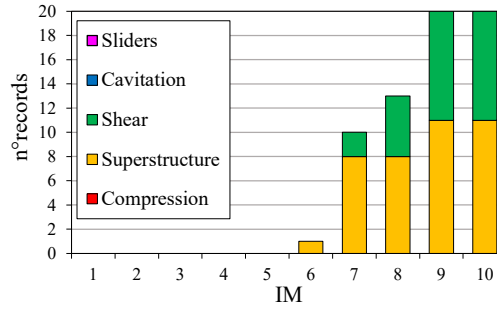
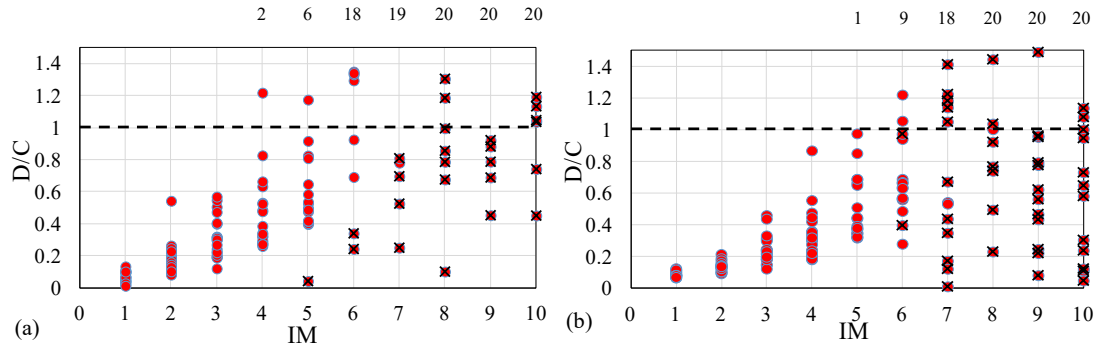


Figure 22. GC results for $HDRB+FSB-NA_{EX}$ ($\alpha=1/2$).

The results relevant to the UPD performance level are summarized in Figure 23 to Figure 25. Generally speaking, existing buildings retrofitted with rubber-based isolation systems works effectively in limiting non-structural damage. Indeed, no failures are observed for seismic intensities much higher than the $IM2$.



- Demand (D) calculated as Maximum Top Displacement registered during the analysis
- ✕ Demand (D) calculated as Current Top Displacement associated to the system collapse

Figure 23. Displacement D/C ratio of the superstructure (UPD) for HDRB- AQ_{EX} : (a) X direction and (b) Y direction.

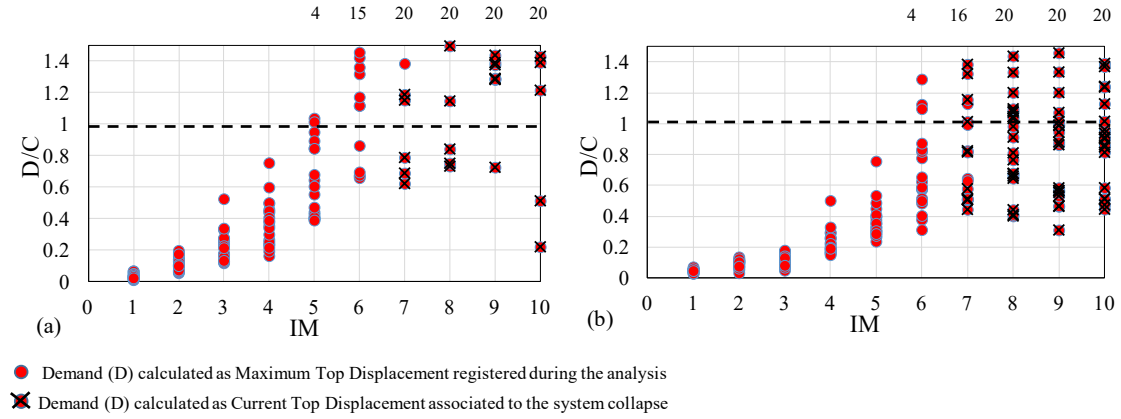


Figure 24. Displacement D/C ratio of the superstructure (UPD) for HDRB+FSB- AQ_{EX} : (a) X direction and (b) Y direction.

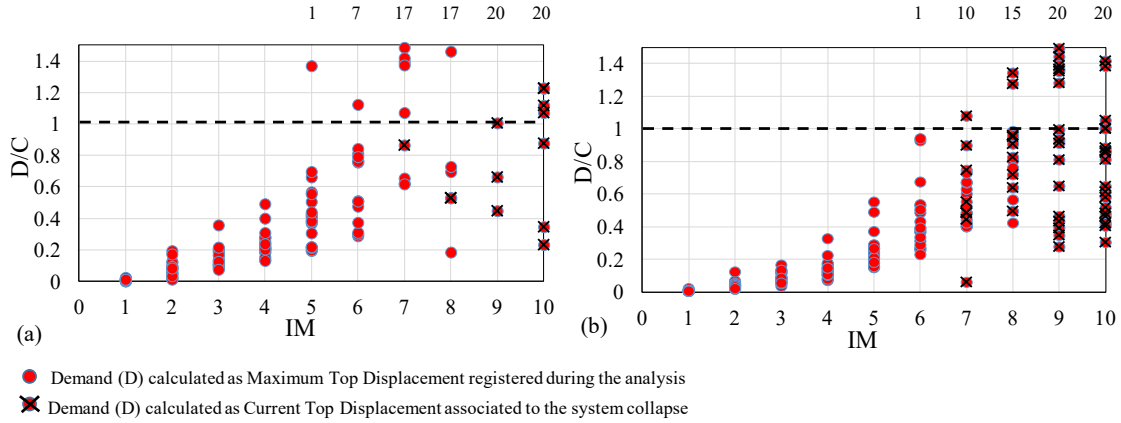


Figure 25. Displacement D/C ratio of the superstructure (UPD) for HDRB+FSB- NA_{EX} : (a) X direction and (b) Y direction.

From the previous results, some preliminary conclusions can be drawn. First, as already argued in [Kitayama and Constantinou 2018] and [Shao et al. 2019], to increase the reliability of base-isolated buildings towards global collapse, the ultimate displacement/strength capacity of both the superstructure and isolation system must be enhanced. Second, while the strength/displacement capacity of the RC superstructure can be deemed to be well known, knowledge regarding the ultimate capacity of the isolation system should be deepened. For example, since the ultimate shear capacity of rubber bearings is currently not tested during the qualification process, mandatory tests may be introduced in the Codes in the near future [Nishi, 2019]. Similarly, the extra-stroke behaviour of the sliders may be experimentally verified. Al-

ternatively, larger safety margins towards the ultimate displacement capacity of the isolation system should be prescribed.

Risk assessment

Results illustrated in the previous sections, concerning the structural system vulnerability, have been used to calculate the annual failure rate, λ_f , for both the *GC* and *UPD* performance levels (Figure 26) and for each case study under consideration, with the R2R software [Baraschino et al. 2019]. The procedure is the classical one reported in [Shome and Cornell, 1999] and corrected conservatively by assuming that for *IM* levels with return periods higher than 100000 years (the maximum considered for *MSA*) the failure is always attained, i.e. by adding 10^{-5} to the annual failure rate computed. More details can be found in [Iervolino et al. 2018]. In Figure 26, the blue markers refer to the new isolated buildings whereas the red ones to the retrofitted buildings. For any building model, light colours refer to past results, obtained by using the *HDR Bearing Element* [Ragni et al. 2018a, Cardone et al. 2019b], while dark colors to results obtained in this study.

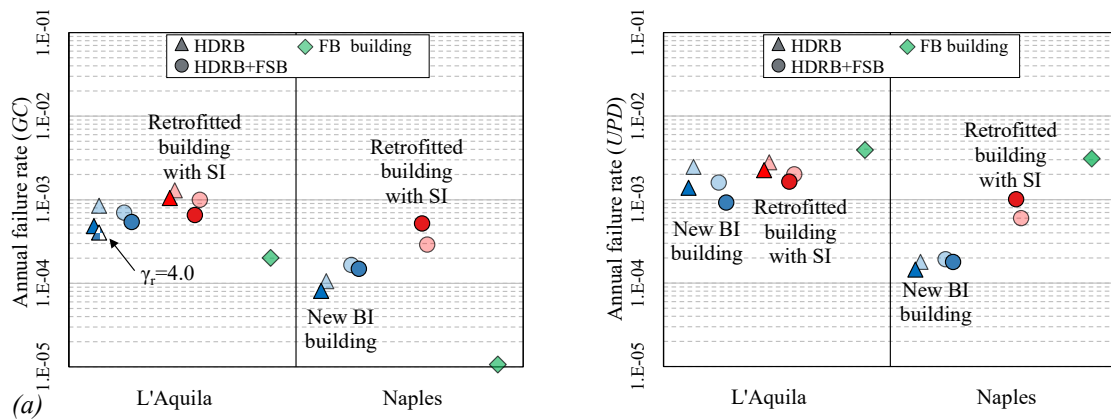


Figure 26. Annual failure rate of GC (a) and UPD (b) performance levels, for different case studies. Lighter markers represent results of past research. BI=base isolated, SI=seismically isolated, FB=fixed base

As can be seen, the annual failure rate in terms of *GC* has a limited variability within all isolated buildings, for a given site. For example, for high seismicity regions (L'Aquila) λ_f is around $\approx 10^{-3}$ for both new and retrofitted buildings with seismic isolation, whereas for the new buildings located in Naples it is around 10^{-4} . These results confirm that, even if the Code prescription should

lead to an equivalent level of security, the hazard of the site strongly influences the actual reliability level, as already highlighted by other studies developed within the RINTC project [Suzuki and Iervolino 2019] or dealing with the risk targeting approach [Fajfar 2018, Gkimprxis et al. 2019, Gkimprxis et al. 2020, Flora et al. 2020]. The influence of the seismic hazard on the annual failure rate is clearly explained by Figure 27 where the hazard curves of L'Aquila and Naples, normalized by the design seismic intensity level ($IM6$, $RP=1000y$), are shown.

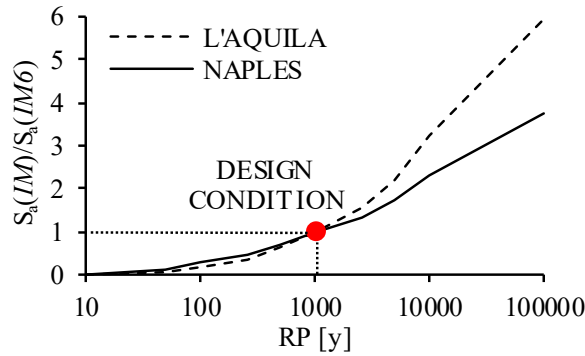


Figure 27. Normalized hazard for L'Aquila and Naples sites

While the curves reported in Figure 27 are similar for return periods lower than 1000y, for higher return periods the hazard related to l'Aquila site increase faster than Naples site, leading to anticipated collapses.

For what concerns the annual failure rate relevant to the UPD performance level, it is worth noting that for the buildings located in L'Aquila the annual failure rate for retrofitted buildings is similar to that of new buildings. The reason is that the *SLD* buildings (existing building designed as fixed-base in compliance with the pre-96 Italian Seismic Code, considering a design base shear around 0.07 the weight of the building) has structural characteristics similar to the new isolated buildings. On the contrary, for the buildings located in Naples the strength of the existing *GLD* buildings (designed for gravity loads only) is significantly lower than the corresponding new isolated buildings. As a consequence, the annual failure rate relevant to the *UPD* performance level for existing buildings located in Naples is higher than for new isolated buildings.

A further remark about the *UPD* performance level is that the obtained annual failure rates are larger than those relevant to the *GC* performance level, but very close to them. This means that

1 the seismic performances of base-isolated buildings are very high in terms of damage control.
2 On the other hand, base-isolated buildings are less reliable than expected in terms of global col-
3 lapse. In other words, base-isolated buildings do not suffer any damage for a wide range of
4 seismic intensities, greater than the associated damage-control design intensity level, but when
5 damage develops the probability of collapse increases rapidly beyond the collapse-prevention
6 design intensity level.

7 For what concerns the modelling approach adopted for rubber isolators, Figure 26 com-
8 pares the annual failure rates derived, for the same base-isolated buildings, using the *HDR Bear-*
9 *ing Element* [Ragni et al. 2018a, Cardone et al. 2019b] with those obtained in this study using
10 the novel *Kikuchi Bearing Element*. In most of the cases, there is a slight tendency towards a re-
11 duction of the failure rates passing from the *HDR* to the *Kikuchi Bearing Element*, but differ-
12 ences are in most of the cases negligible both for *GC* and *UPD* performance levels.

13 Finally, comparing the annual failure rate of base-isolated buildings with the correspond-
14 ing values relevant to similar fixed-base buildings (6-storeys RC frame buildings with same ge-
15 ometry, same reference seismic Code, etc.), one can find that fixed-base structures have an an-
16 nual failure rate lower than base-isolated structures in terms of *GC* performance level, but sig-
17 nificantly larger in terms of *UPD* performance levels, in accordance with the findings of other
18 authors [Kitayama and Constantinou 2018, Shao et al. 2019]. Obviously, also in this case results
19 are significantly site-specific, i.e. strongly affected by the local seismic hazard.

20 At first sight, the obtained results point out that all base-isolated buildings are character-
21 ized by similar reliability levels for both *UPD* and *GC* performance levels, whereas fixed-base
22 structures exhibit a *UPD* reliability level lower than base-isolated buildings but a *GC* reliability
23 level significantly greater. Nevertheless, two important remarks should be done. The first one is
24 that in the *UPD* definition no considerations about the floor accelerations are made, because on-
25 ly the in-plane damage of infills is considered as monitored damaging parameter. Consequently,
26 the significant damage reduction due to the lower floor accelerations experienced by isolated
27 structures is not taken into account in this study. Some works concerning the out-of-plane be-
28 haviour of masonry infills are currently in progress [Gesualdi et al. 2020] within the RINTC

project and could be integrated in the UPD performance level in the near future, as also consideration about other non-structural components (suspended ceilings, furniture, acceleration sensitive devices).

The second important remark is that the comparison previously carried out between fixed-base and base-isolated structures has a qualitative nature because the two cases consider a different hazard description. In details, different choices made for the *GMPE* used during the hazard assessment may have affected the results. Indeed, for fixed-base structures the *GMPE* of Ambraseys [Ambraseys *et al.*, 1996] has been used. It is valid for periods lower than $T_{max} = 2\text{s}$ and uses as intensity measure the maximum spectral acceleration between the signals registered in the two horizontal directions (usually referred to as Sa_{larger} , according to the notation of [Boore and Kishida, 2017]). Since the isolation period is always higher than the period limit of the *GMPE* of Ambraseys, the *GMPE* by Akkar and Bommer has been used for base-isolated buildings, and as a consequence the geometrical mean of the spectral acceleration of the two horizontal components (Sa_{GM}) has been used as intensity measure.

A bias between the Code hazard (considered in the design) and the effective hazard associated with the seismic input (used for the risk assessment) may have further influenced the results.

For this reason, a comparison between the two hazard curves used in the analyses has been carried out, as shown in Figure 28. An intensity measure conversion has been applied to the *GMPE* of Akkar and Bommer, by using the relationships suggested in [Beyer and Bommer 2006], in order to compare the hazard curves derived with the two approaches. In particular, the comparison between the direct hazard curves of Ambraseys and the converted direct hazard curves of Akkar and Bommer is made for two reference periods, i.e. (a) $T=0.5\text{ s}$ and (b) $T=2\text{ s}$. From the comparison, it is evident that the two hazard curves are almost coincident for short periods, whereas for larger periods the Akkar and Bommer hazard curve, used for base-isolated buildings, is significantly higher than the Ambraseys hazard curve used for fixed-base buildings. In the same figure, the “real” hazard curve used in the analyses has been also reported. It has been directly derived from the sets of records selected for *NTHA*, following the procedure

illustrated in [Lin et al. 2013, NIST 2011]. It is worth noting that that even if the conditioning period (T^*) is different from the selected periods of the hazard curves, empirical and direct hazards are very close each other due to the insensitivity to the conditioning period of the empirical hazard curves when CS-based ground motion selection is used [Lin et al. 2013]. It is then confirmed that the ground motion selection used for base-isolated structures, based on the *GMPE* of Akkar and Bommer, is consistent with the direct hazard curve of Akkar and Bommer and larger than the direct hazard curve of Ambraseys for large periods. It should be also noted that the selected fixed-base building has an elastic period around $T=0.5$ s, however its effective period of vibration significantly increases with the earthquake intensity level due to the strong nonlinear behaviour of the RC frame [Lin et al. 2013]. As a consequence, the seismic hazard for large periods may have a significant influence on the seismic response of fixed-base buildings. Obviously, to exactly evaluate how much this difference in the hazard influences the results in terms of the annual failure rate, fixed-based structures should be analysed with a set of ground motions consistent with the Akkar and Bommer hazard curve or, alternatively, both base-isolated structures and fixed-base structures should be analysed using set of records consistent with a hazard curve defined in a wide range of periods, e.g. defining the hazard curve by the Lanzano *GMPE* [Lanzano et al. 2019] (see also [Micozzi 2020]).

Finally, in Figure 28 the Code hazard [CS.LL.PP. 2019] used in the design stage is also reported (and called *NTC*). Although the *NTC* hazard curve is steeper than both the direct hazard curves and the empirical ones, there is a quite good agreement between *NTC* hazard and Akkar and Bommer hazard calculated from the record selection in the range of the design annual rate of exceedance ($RP = 1000y$ or $\lambda=10^{-3}$).

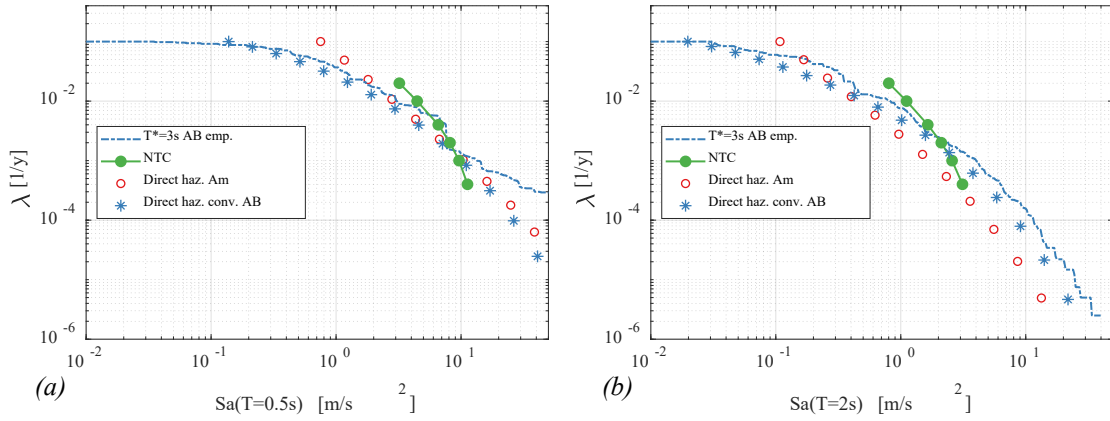


Figure 28. Hazard curves for the site of L'Aquila: (a) $S_a(T=0.5)$, (b) $S_a(T=2.0)$ directly computed from hazard assessment from Ambraseys (Am) and Akkar and Bommer (AB) GMPEs, empirically computed from record selection (emp) conditioned at $T^*=3s$ and code hazard (NTC)

Conclusions

An insight on the response under different seismic intensity levels and on the seismic risk of rubber-based isolated buildings has been presented. The analyses have been performed within the *RINTC* research project on both new designed isolated buildings and existing RC buildings retrofitted with seismic isolation. The isolation systems have been designed in accordance with the current Italian Seismic Code and all the case studies have been assessed by means of multi-stripe nonlinear time history analysis, computing the annual failure rate for two performance levels, namely *Global Collapse (GC)* and *Usability Preventing Damage (UPD)*. A multi-criteria approach has been followed for the definition of the aforesaid performance levels as base-isolated buildings are in-series systems (being composed by the isolation system and the super-structure) and isolation devices can undergo different failure modes.

One of the most advanced numerical models currently available for the description of the nonlinear cyclic behaviour of *HDRBs* (namely the *Kikuchi Bearing Element*) has been used in the analyses, due to its capability of simulating the behaviour of *HDRBs* under large displacements and high axial loads. The model parameters have been calibrated against experimental results of an extensive experimental investigation.

The results of this study show that Code-conforming base-isolated structures work effectively in limiting the probability of damage, but they may exhibit a low margin with respect to the global collapse of structure, especially for high seismicity regions. On the other hand, code-

conforming fixed-base RC buildings show larger annual failure rates relevant to damage prevention but lower annual failure rates regarding the collapse.

The new results obtained with the *Kikuchi Bearing element* does not seem to significantly modify, at least for the examined case studies, the numerical prediction of the annuals failure rates in terms of both *Global Collapse* and *Usability Preventing Damage* in comparison to already adopted model in past research, thus confirming the robustness of the analysis approach.

Finally, the results derived from risk assessment have been critically examined and compared in the light of the different hazard definition for base-isolated and fixed-base structures. A common hazard, suitable for both base-isolated and fixed-base structure, may lead to a reduced gap between the annual failure rate in terms of *GC* performance level observed for base-isolated and fixed-base structures. Alternatively, further investigations about the reliability of simplified methods based on the fragility curves conversion should be carried out.

Acknowledgements

The study presented in this article was developed within the activities of the ReLUIS-DPC 2019-2021 research program, funded by the Italian Dept. of Civil Protection. The authors are grateful to Prof. Iunio Iervolino (University of Naples, Federico II) for his valuable assistance in deriving hazard curves and for the helpful discussion on risk assessment.

References

- Akkar, S., Bommer, J.J. [2010] Empirical Equations for the Prediction of PGA, PGV, and Spectral Accelerations in Europe, the Mediterranean Region, and the Middle East. *Seismological Research Letters* 81, 195–206. <https://doi.org/10.1785/gssrl.81.2.195>
- Ambraseys, N.N., Simpson, K.A., Bommer, J.J. [1996] Prediction of horizontal response spectra in Europe. *Earthquake Engineering & Structural Dynamics* 25, 371–400. doi:10.1002/(SICI)1096-9845(199604)25:4<371::AID-EQE550>3.0.CO;2-A.
- Aslani, H, Miranda, E (2005). Probabilistic earthquake loss estimation and loss disaggregation in buildings. Report No. 157. The John A. Blume Earthquake Engineering Center, Department of Civil and Environmental Engineering, Stanford University, Stanford, CA, USA.
- Beyer, K., & Bommer, J. J. (2006). Relationships between median values and between aleatory variabilities for different definitions of the horizontal component of motion. *Bulletin of the Seismological Society of America*, 96(4A), 1512-1522
- Baraschino R., Baltzopoulos G., Iervolino I. [2019] R2R-EU: Software for fragility fitting and evaluation of estimation uncertainty in seismic risk analysis. *Soil Dynamics and Earthquake Engineering*.

- 1 Brandonisio, G., Ponzo, F., Mele, E., Luca, A.D. [2017] Experimental tests of elastomeric isolators: influence of vertical load V and of secondary shape factor, Proc. of 17th ANIDIS Conference, Pisa, Italy
- 4 Bridgestone Corporation [2017] Seismic isolation product line-up.
- 5 Boore, D.M., Kishida, T. [2017] Relations between Some Horizontal- Component Ground-Motion Intensity Measures Used in Practice. Bulletin of the Seismological Society of America 107, 334–343.
- 7 <https://doi.org/10.1785/0120160250>
- 8 Camata, G., Celano, F., Risi, M.T.D., Franchin, P., Magliulo, G., Manfredi, V., Masi, A., Mollaioli, F., Noto, F., Ricci, P., Spacone, E., Terrenzi, M., Verderame, G.M. [2017]. RINTC project: nonlinear dynamic analyses of italian code-conforming reinforced concrete buildings for risk of collapse assessment, (COMPDYN 2017), Rhodes Island, Greece.
- 12 <https://doi.org/10.7712/120117.5507.17050>
- 13 Cardone, D., Flora, A., Gesualdi, G., [2013] Inelastic response of RC frame buildings with seismic isolation. Earthquake Engineering & Structural Dynamics 42, 871–889.
- 15 <https://doi.org/10.1002/eqe.2250>
- 16 Cardone, D., Flora, A., [2016] An alternative approach for the seismic rehabilitation of existing RC buildings using seismic isolation. Earthquake Engineering & Structural Dynamics 45, 91–111.
- 18 <https://doi.org/10.1002/eqe.2618>
- 19 Cardone, D., Perrone, G., Piesco, V. [2019a] Developing collapse fragility curves for base-isolated buildings. Earthquake Engng Struct Dyn; 48: 78– 102. <https://doi.org/10.1002/eqe.3126>
- 21 Cardone, D., Conte, N., Dall'Asta, A., Di Cesare, A., Flora, A., Lamarucciola, N., Micozzi, F., Ponzo, F., Ragni, L. [2019b] RINTC-e project: the seismic risk of existing italian rc buildings retrofitted with seismic isolation, in: Proceedings of the 7th International Conference on Computational Methods in Structural Dynamics and Earthquake Engineering (COMPDYN 2019), Crete, Greece, pp. 3403–3421. <https://doi.org/10.7712/120119.7156.19921>
- 26 Cardone, D., Gesualdi, G., Perrone, G. [2019c] Cost-Benefit Analysis of Alternative Retrofit Strategies for RC Frame Buildings, Journal of Earthquake Engineering, 23:2, 208–
- 28 241, DOI: [10.1080/13632469.2017.1323041](https://doi.org/10.1080/13632469.2017.1323041).
- 29 CEN-EN [2005] Design of structures for earthquake resistance, part 1, Eurocode 8, Brussels.
- 30 Constantinou, M.C., Mokha, A., Reinhorn, A. [1990] "Teflon bearings in base isolation. II: Modeling." Journal of Structural Engineering (ASCE) 1990; 116(2): 455-474
- 32 CS.LL.PP. [2018] “Aggiornamento delle norme tecniche per le costruzioni”, Gazzetta Ufficiale della Repubblica Italiana 42. (In Italian.)
- 34 CS.LL.PP. [2019] Circolare n. 7 - Istruzioni per l'applicazione dell' “Aggiornamento delle Norme tecniche per le costruzioni” di cui al decreto ministeriale 17 gennaio 2018, Gazzetta Ufficiale della Repubblica Italiana 35. (In Italian.)
- 37 De Risi, M.T., Ricci, P., Verderame, G.M. [2017] Modelling exterior unreinforced beam-column joints in seismic analysis of non-ductile RC frames. Earthquake Engineering & Structural Dynamics 46, 899–923. <https://doi.org/10.1002/eqe.2835>
- 40 Decanini, L.D., Liberatore, L., Mollaioli, F. [2014] Strength and stiffness reduction factors for infilled frames with openings. Earthq. Eng. Eng. Vib. 13, 437–454. <https://doi.org/10.1007/s11803-014-0254-9>
- 43 D.M. 30/5/1974. Decreto Ministeriale 30 maggio 1974. Norme tecniche per la esecuzione delle opere in cemento armato normale e precompresso e per le strutture metalliche. Gazzetta Ufficiale n. 198 del 29 luglio 1974. (in Italian).
- 46 D.M. 24/1/1986. Decreto Ministeriale 24 gennaio 1986. Norme tecniche relative alle costruzioni antisismiche. Gazzetta Ufficiale n. 108 del 12 maggio 1986. (in Italian).
- 48 D.M. 14/2/1992. Decreto Ministeriale 14 febbraio 1992. Norme tecniche per le opere in c.a. normale e precompresso e per le strutture metalliche. Gazzetta Ufficiale n. 65 del 18 marzo 1992. (in Italian).

- 1 Dolce, M., Ponzo, F.C., Di Cesare, A., Arleo, G. [2010] Progetto di edifici con isolamento sismico. (In
2 Italian). Iuss Press, Pavia, Italy
- 3 EN15129 [2009] Antiseismic Devices, European Committee for Standardization, Brussels, Belgium.
- 4 Fajfar, P., [2018] Analysis in seismic provisions for buildings: past, present and future: The fifth Prof.
5 Nicholas Ambraseys lecture. Bull Earthquake Eng 16, 2567–2608.
6 <https://doi.org/10.1007/s10518-017-0290-8>
- 7 Flora, A., Perrone, G., Cardone, D. [2020] Developing risk-target based design approaches for base iso-
8 lated Buildings. Proceedings of the 17th World Conference on Earthquake Engineering,
9 17WCEE Sendai, Japan - September 13th to 18th 2020
- 10 Gesualdi, G., Viggiani, L.R.S., Cardone, D. [2020] Seismic performance of RC frame buildings account-
11 ing for the out-of-plane behavior of masonry infills. Bull Earthquake Eng 18, 5343–5381.
12 <https://doi.org/10.1007/s10518-020-00904-1>
- 13 Gkimprxis, A., Tubaldi, E., Douglas, J. [2019] Comparison of methods to develop risk-targeted seismic
14 design maps. Bull Earthquake Eng 17, 3727–3752. <https://doi.org/10.1007/s10518-019-00629-w>
- 15 Gkimprxis, A., Tubaldi, E., Douglas, J. [2020] Evaluating alternative approaches for the seismic design
16 of structures. Bull Earthquake Eng. <https://doi.org/10.1007/s10518-020-00858-4>
- 17 Grant, D.N., Fenves, G.L., Whittaker, A.S. [2004] Bidirectional modelling of high-damping rubber bear-
18 ings. Journal of Earthquake Engineering 8, 161–185.
19 <https://doi.org/10.1080/13632460409350524>
- 20 Ibarra, L.F., Krawinkler, H., 2005. Global Collapse of Frame Structures under Seismic Excitations. Rep.
21 No. TB 152, The John A. Blume Earthquake Engineering Center.
- 22 Ibarra, L.F., Medina, R.A., Krawinkler, H. [2005] Hysteretic models that incorporate strength and stiff-
23 ness deterioration. Earthquake Engng Struct. Dyn. 34, 1489–1511.
24 <https://doi.org/10.1002/eqe.495>
- 25 Iervolino, I., Dolce, M. [2018]. Foreword to the Special Issue for the RINTC (The Implicit Seismic Risk
26 of Code-Conforming Structures) Project. Journal of Earthquake Engineering 1–4.
27 <https://doi.org/10.1080/13632469.2018.1543697>
- 28 Iervolino, I., Spillatura, A., Bazzurro, P. [2018]. Seismic Reliability of Code-Conforming Italian Build-
29 ings. Journal of Earthquake Engineering 22, 5–27.
30 <https://doi.org/10.1080/13632469.2018.1540372>
- 31 Ishii, K., Kikuchi, M. [2019]. Improved numerical analysis for ultimate behavior of elastomeric seismic
32 isolation bearings. Earthquake Engng Struct Dyn 48, 65–77. <https://doi.org/10.1002/eqe.3123>
- 33 Jalayer, F. [2003] “Direct Probabilistic seismic analysis: implementing nonlinear dynamic assess-
34 ment,”Ph.D. thesis, Department of Civil and Environmental Engineering, Stanford University,
35 Stanford,CA, USA.
- 36 Kelly, J.M. [1997] Earthquake-resistant design with rubber. Springer London Ltd, .
- 37 Kikuchi, M., Aiken, I.D. [1997]. An Analytical Hysteresis Model for Elastomeric Seismic Isolation Bear-
38 ings. Earthquake Engineering & Structural Dynamics 26, 215–231.
39 [https://doi.org/10.1002/\(SICI\)1096-9845\(199702\)26:2<215::AID-EQE640>3.0.CO;2-9](https://doi.org/10.1002/(SICI)1096-9845(199702)26:2<215::AID-EQE640>3.0.CO;2-9)
- 40 Kikuchi, M., Nakamura, T., Aiken, I.D. [2010] Three-dimensional analysis for square seismic isolation
41 bearings under large shear deformations and high axial loads. Earthquake Engng. Struct. Dyn.
42 39, 1513–1531. <https://doi.org/10.1002/eqe.1042>
- 43 Kitayama, S., Constantinou, M.C., [2018] “Collapse performance of seismically isolated buildings de-
44 signed by the procedures of ASCE/SEI 7” Engineering Structures 164, 243–258.
45 <https://doi.org/10.1016/j.engstruct.2018.03.008>
- 46 Kitayama, S., Constantinou, M.C. [2019] Probabilistic seismic performance assessment of seismically
47 isolated buildings designed by the procedures of ASCE/SEI 7 and other enhanced criteria. Engi-
48 neering Structures 179, 566–582. <https://doi.org/10.1016/j.engstruct.2018.11.014>
- 49 Koh CG, Kelly JM. [1988] A simple mechanical model for elastomeric bearings used in base isolation.
50 International. Journal of Mechanical Sciences; 30:933–943.

- 1 Koh, C. G., and Kelly, J. M. [1986] "Effects of axial load on elastomeric bearings." UCB/EERC-86/12,
2 Earthquake Engrg. Res. Ctr., University of California, Berkeley, Calif.
- 3 Koh, C.G., Balendra, T. [1989] Seismic response of base isolated buildings including p- Δ effects of isola-
4 tion bearings. *Earthquake Engineering & Structural Dynamics* 18, 461–473.
5 <https://doi.org/10.1002/eqe.4290180402>
- 6 Kumar, M., Whittaker, A.S., Constantinou, M.C. [2014]. An advanced numerical model of elastomeric
7 seismic isolation bearings: An advanced numerical model of elastomeric seismic isolation bear-
8 ings. *Earthquake Engineering & Structural Dynamics* 43, 1955–1974.
9 <https://doi.org/10.1002/eqe.2431>
- 10 Lanzano, G., Luzi, L., Pacor, F., Felicetta, C., Puglia, R., Sgobba, S., D'Amico, M., [2019]. A Revised
11 Ground-Motion Prediction Model for Shallow Crustal Earthquakes in Italy. *Bulletin of the*
12 *Seismological Society of America* 109, 525–540. <https://doi.org/10.1785/0120180210>
- 13 Lin, T., Haselton, C.B., Baker, J.W. [2013] Conditional spectrum-based ground motion selection. Part I:
14 Hazard consistency for risk-based assessments. *Earthquake Engineering & Structural Dynamics*
15 42, 1847–1865. <https://doi.org/10.1002/eqe.2301>
- 16 McKenna, F. [2011] OpenSees: A Framework for Earthquake Engineering Simulation. *Computing in*
17 *Science Engineering* 13, 58–66. <https://doi.org/10.1109/MCSE.2011.66>
- 18 Micozzi, F. [2020] Seismic reliability of buildings isolated with rubber bearings. Ph.D. Dissertation,
19 University of Camerino, Italy. <http://hdl.handle.net/11581/446064>
- 20 Monelli, D., Pagani, M., Weatherill, G., Silva, V., Crowley, H. [2012] The hazard component of Open-
21 Quake: The calculation engine of the Global Earthquake Model. *Proc. of 15WCEE – 15th World*
22 *Conference on Earthquake Engineering*, Lisbon, Portugal.
- 23 Monzon, E.V., Buckle, I.G., Itani, A.M. [2016]. Seismic Performance and Response of Seismically Iso-
24 lated Curved Steel I-Girder Bridge. *J. Struct. Eng.* 142, 04016121.
25 [https://doi.org/10.1061/\(ASCE\)ST.1943-541X.0001594](https://doi.org/10.1061/(ASCE)ST.1943-541X.0001594)
- 26 Mullins L. [1969] Softening of rubber by deformation, *Rubber Chemistry and Technology*, 42(1): 339-
27 362.
- 28 Naeim, F., Kelly, J.M., [1999] "Design of Seismic Isolated Structures". John Wiley & Sons, Inc., Hobo-
29 ken, NJ, USA. <https://doi.org/10.1002/9780470172742>
- 30 Nakazawa, T., Kishiki, S., Qu, Z., Miyoshi, A., Wada, A., [2011]. Fundamental study on probabilistic
31 evaluation of the ultimate state of base isolated structures. *Nihon Kenchiku Gakkai Kozokei*
32 *Ronbunshu* 76, 745–754. <https://doi.org/10.3130/aijs.76.745>
- 33 Nishi, T., Suzuki, S., Aoki, M., Sawada, T., Fukuda, S. [2019] International investigation of shear dis-
34 placement capacity of various elastomeric seismic-protection isolators for buildings. *J Rubber*
35 *Res* 22, 33–41. <https://doi.org/10.1007/s42464-019-00006-x>
- 36 NIST [2011] Selecting and scaling earthquake ground motions for performing response-history analyses,
37 NIST GCR 11-917-15. Technical Report, prepared by the NEHRP Consultants Joint Venture for
38 the National Institute of Standards and Technology: Gaithersburg, Maryland.
- 39 prEN 1337-5 [2005] Structural bearings - Part 5: Pot bearings. European Committee for Standardization,
40 Brussels
- 41 Ragni, L., Cardone, D., Conte, N., Dall'Asta, A., Cesare, A.D., Flora, A., Leccese, G., Micozzi, F.,
42 Ponzio, C. [2018a] Modelling and Seismic Response Analysis of Italian Code-Conforming Base-
43 Isolated Buildings. *Journal of Earthquake Engineering*, 1–33. Vol. 22(sup2), 2018, 198-230
44 <https://doi.org/10.1080/13632469.2018.1527263>
- 45 Ragni, L., Tubaldi, E., Dall'Asta, A., Ahmadi, H., Muhr, A. [2018b] Biaxial shear behaviour of HDNR
46 with Mullins effect and deformation-induced anisotropy. *Engineering Structures* 154, 78–92.
47 <https://doi.org/10.1016/j.engstruct.2017.10.060>
- 48 ReLUIS-RINTC Workgroup [2018]. Results of the 2015-2017 RINTC project. ReLUIS-RINTC report,
49 ReLUIS, Naples, Italy. Available at <http://www.reluis.it>.
- 50 Ricci, P., Manfredi, V., Noto, F., Terrenzi, M., Petrone, C., Celano, F., De Risi, M.T., Camata, G., Fran-
51 chin, P., Magliulo, G., Masi, A., Mollaioli, F., Spacone, E., Verderame, G.M. [2018] Modeling

- and Seismic Response Analysis of Italian Code-Conforming Reinforced Concrete Buildings. *Journal of Earthquake Engineering* 22, 105–139. <https://doi.org/10.1080/13632469.2018.1527733>
- Ricci, P., Manfredi, V., Noto, F., Terrenzi, M., De Risi, M.T., Di Domenico, M., Camata, G., Franchin, P., Masi, A., Mollaioli, F., Spacone, E., Verderame, G.M. [2019] RINTC-e: towards seismic risk assessment of existing residential reinforced concrete buildings in Italy, in: *Proceedings of the 7th International Conference on Computational Methods in Structural Dynamics and Earthquake Engineering (COMPDYN 2019)*, Crete, Greece, pp. 554–576. <https://doi.org/10.7712/120119.6939.20040>
- Sassun, K., Sullivan, T.J., Morandi, P., Cardone, D. [2016] Characterising the in-plane seismic performance of infill masonry. *Bulletin of the New Zealand Society for Earthquake Engineering* 49(1), 100–117.
- Scozzese, F., Tubaldi, E., Dall'Asta, A. [2020] Assessment of the effectiveness of Multiple-Stripe Analysis by using a stochastic earthquake input model. *Bull Earthquake Eng.* <https://doi.org/10.1007/s10518-020-00815-1>
- Shao, B., Mahin, S.A., Zayas, V. [2019] Achieving targeted levels of reliability for low-rise seismically isolated structures. *Soil Dynamics and Earthquake Engineering* 125, 105744. <https://doi.org/10.1016/j.soildyn.2019.105744>
- Shome, N., Cornell, C.A. [1999] Probabilistic seismic demand analysis of nonlinear structures. Technical Report RMS-35, RMS Program: Stanford, CA.
- Spillatura, A. [2018] From Record Selection to Risk Targeted Spectra for Risk based Assessment and Design. Ph.D. Thesis, Dipartimento di Costruzioni e Infrastrutture, Istituto Universitario degli Studi Superiori (IUSS), Pavia, Italy.
- Suzuki A., Iervolino I. (2019) Seismic fragility of code-conforming Italian buildings based on SDoF approximation. *Journal of Earthquake Engineering*. DOI:10.1080/13632469.2019.1657989
- Takaoka, E., Takenaka, Y., Nimura, A. [2011] Shaking table test and analysis method on ultimate behavior of slender base-isolated structure supported by laminated rubber bearings. *Earthquake Engng. Struct. Dyn.* 40, 551–570. <https://doi.org/10.1002/eqe.1048>
- Tubaldi, E., Ragni, L., Dall'Asta, A., Ahmadi, H., Muhr, A. [2017] Stress softening behaviour of HDNR bearings: modelling and influence on the seismic response of isolated structures: Stress Softening Behaviour of HDNR Bearings. *Earthquake Engineering & Structural Dynamics*. <https://doi.org/10.1002/eqe.2897>
- Wada, A., Hirose, K. [1987] Building frames subjected to 2D earthquake motion. *Proceedings, Structures Congress '89*, ASCE, San Francisco, CA, 388–397.
- Warn GP. The coupled horizontal-vertical response of elastomeric and lead rubber seismic isolation bearings. Ph.D. Dissertation. Buffalo (NY): The State University of New York at Buffalo; 2006.
- Yamamoto, S., Kikuchi, M., Ueda, M., Aiken, I.D. [2009] A mechanical model for elastomeric seismic isolation bearings including the influence of axial load. *Earthquake Engng Struct. Dyn.* 38, 157–180. <https://doi.org/10.1002/eqe.847>